

Geological Society of America Bulletin

Evidence for middle Eocene and younger land emergence in central Panama: Implications for Isthmus closure

Camilo Montes, A. Cardona, R. McFadden, S.E. Morón, C.A. Silva, S. Restrepo-Moreno, D.A. Ramírez, N. Hoyos, J. Wilson, D. Farris, G.A. Bayona, C.A. Jaramillo, V. Valencia, J. Bryan and J.A. Flores

Geological Society of America Bulletin published online 13 January 2012;
doi: 10.1130/B30528.1

Email alerting services

click www.gsapubs.org/cgi/alerts to receive free e-mail alerts when new articles cite this article

Subscribe

click www.gsapubs.org/subscriptions/ to subscribe to Geological Society of America Bulletin

Permission request

click <http://www.geosociety.org/pubs/copyrt.htm#gsa> to contact GSA

Copyright not claimed on content prepared wholly by U.S. government employees within scope of their employment. Individual scientists are hereby granted permission, without fees or further requests to GSA, to use a single figure, a single table, and/or a brief paragraph of text in subsequent works and to make unlimited copies of items in GSA's journals for noncommercial use in classrooms to further education and science. This file may not be posted to any Web site, but authors may post the abstracts only of their articles on their own or their organization's Web site providing the posting includes a reference to the article's full citation. GSA provides this and other forums for the presentation of diverse opinions and positions by scientists worldwide, regardless of their race, citizenship, gender, religion, or political viewpoint. Opinions presented in this publication do not reflect official positions of the Society.

Notes

Advance online articles have been peer reviewed and accepted for publication but have not yet appeared in the paper journal (edited, typeset versions may be posted when available prior to final publication). Advance online articles are citable and establish publication priority; they are indexed by GeoRef from initial publication. Citations to Advance online articles must include the digital object identifier (DOIs) and date of initial publication.

Evidence for middle Eocene and younger land emergence in central Panama: Implications for Isthmus closure

Camilo Montes^{1,2,†}, A. Cardona^{1,3}, R. McFadden¹, S.E. Morón¹, C.A. Silva¹, S. Restrepo-Moreno^{1,4}, D.A. Ramírez¹, N. Hoyos¹, J. Wilson¹, D. Farris⁵, G.A. Bayona⁶, C.A. Jaramillo¹, V. Valencia⁷, J. Bryan⁸, and J.A. Flores⁹

¹Smithsonian Tropical Research Institute, Box 0843-03092, Balboa, Ancón, Republic of Panamá

²Geociencias, Universidad de los Andes, Calle 1A # 18A-10, Edificio IP, Bogotá DC, Colombia

³Ingeniería de Petróleos, Universidad Nacional de Colombia, Carrera 80 No. 65-223, Medellín, Colombia

⁴Department of Geological Sciences, University of Florida, 241 Williamson Hall, Gainesville, 24 Florida 32611, USA

⁵Department of Earth, Ocean and Atmospheric Science, Florida State University, 1017 26 Academic Way, Tallahassee, Florida 32306-4520, USA

⁶Corporación Geológica Ares, Calle 44A # 53-96, Bogotá, Colombia

⁷Department of Geosciences, University of Arizona, Gould-Simpson Building #77, 1040 E Street, Tucson, Arizona 85721, USA

⁸Geology/Oceanography, Northwest Florida State College, 100 College Boulevard, Niceville, Florida 32578, USA

⁹Facultad de Ciencias, Departamento de Geología, Universidad de Salamanca, 37008 Salamanca, Spain

ABSTRACT

The rise of the Isthmus of Panama, linked to a number of climatic, paleoceanographic, and biological events, has been studied mostly from indirect, often distal, geochemical and biotic evidence. We have upgraded existing geologic mapping in central Panama with more than 2000 field stations, over 40 petrographic analyses, and more than 30 new geochronological and thermochronological analyses. This data set suggests that the isthmus was an uninterrupted chain above sea level from late Eocene until at least late Miocene times. The basement complex of central Panama is a folded-faulted, ~3-km-thick arc sequence, intruded by granitoid bodies and onlapped by mildly deformed upper Eocene and Oligocene strata. Six U/Pb zircon ages in the granitoids—along with published geochronological data—reveal intense late Paleocene to middle Eocene magmatism (58–39 Ma), a temporary cessation of magmatic activity between 38 and 27 Ma, and renewed magmatism between 25 and 15 Ma in a position ~75 km south of the former magmatic axis. Thermochronological analyses in zircon (eight U-Th/He ages), and in apatite crystals (four U-Th/He ages and nine fission-track ages) obtained from a subset of 58–54 Ma granitoid bodies record a concordant Lutetian-age (47–42 Ma) cooling from ~200 °C to ~70 °C in ~5 m.y., and cooling be-

low ~40 °C between 12 and 9 Ma. Cooling is linked to exhumation by an angular unconformity that separates the deformed basement complex below from mildly deformed, upper Eocene to Oligocene terrestrial to shallow-marine strata above. Exhumation and erosion of the basement complex are independently confirmed by lower Miocene strata that have a detrital zircon signature that closely follows the central Panama basement complex age distribution. These results greatly restrict the width and depth of the strait separating southern Central America from South America, and challenge the widely accepted notion that the Central American Seaway closed in late Pliocene time, when the ice age began.

INTRODUCTION

The emergence of the Isthmus of Panama and separation of Pacific-Caribbean waters has been interpreted as the trigger for major climatic and biotic changes, including the onset of Northern Hemisphere glaciations, the strengthening of the Gulf Stream current (e.g., Burton et al., 1997; Haug et al., 2001; Lear et al., 2003), the Great American Interchange of land mammals (Marshall et al., 1982), and an increase in Caribbean molluscan diversity (Jackson et al., 1993). Isotopic, geochemical, and faunal changes in sedimentary strata on both sides of the isthmus have been used to indirectly narrow the timing of emergence and closure to between ca. 7 and 3.5 Ma (Keigwin, 1978, 1982; Duque-Caro, 1990; Coates et al., 1992, 2004; Collins

et al., 1996; Kameo and Sato, 2000; Beu, 2001; Newkirk and Martin, 2009). Some of the evidence for timing, however, may also be interpreted to show no causal relationship to isthmus closure (see review by Molnar, 2008), partially because most studies rely on distal records of isotopic, chemical, or faunal changes, which are then correlated to a Pliocene isthmus closure.

The paleogeographic evolution of the isthmus strait can additionally be constrained using: (1) land-mammal isthmian faunas (Whitmore and Stewart, 1965; Kirby and MacFadden, 2005) that call for a peninsula connected to North America by the early Miocene; (2) geochemistry of isthmian volcanic products that suggest an early Miocene initiation of collision with South America (Farris et al., 2011); and (3) regional palinspastic reconstructions (Wadge and Burke, 1983; Pindell and Kennan, 2009) that allow only a narrow gap, or no gap, between the Central American volcanic arc and northwestern South America during Neogene times, albeit with no information on the degree of land emergence. Molecular biology studies of saltwater-intolerant frogs (Weigt et al., 2005), freshwater fish (Birmingham and Martin, 1998), and plants (Cody et al., 2010) allow early exchange times in the middle to late Miocene, well before the presumed formation of the land bridge. An understanding of the timing and extent of emergence in the central part of the isthmus from its onshore geologic record is therefore a fundamental component of global paleoceanographic and paleoclimatic modeling, molecular biology, and biogeography efforts.

[†]E-mail: cmontes@uniandes.edu.co

The purpose of this paper is to: (1) document the timing and style of deformation in the isthmus using geologic mapping; (2) better document the timing of magmatic activity in the isthmus using U/Pb geochronology, and the role of these magmatic products in isthmus emergence using thermochronological data; and (3) study the origin and provenance record of Eocene to Miocene terrestrial deposits (e.g., Gatuncillo and Cucaracha Formations; Woodring, 1957). Here, we first refine existing mapping and lithological and geochronological characterization of the volcanoclastic and plutonic basement, and the overlying sedimentary and volcanoclastic cover in central Panama. We then present new thermochronological data in basement rocks, document a late Eocene to Oligocene unconformity, and examine the

detrital geochronology signature preserved in lower Miocene strata. We interpret these data as the record of middle Eocene and younger deformation, exhumation, and erosion processes in the Isthmus of Panama, which greatly restricted the width of the seaway separating the Pacific and Caribbean waters since at least early Miocene times.

GEOLOGIC SETTING

The Isthmus of Panama is located east of the easternmost Central American modern volcano El Valle Volcano (de Boer *et al.*, 1991; Defant *et al.*, 1991a) and west of the Uraba Gulf in western Colombia (Fig. 1). The Isthmus of Panama, barely 100 km across, traces a curve that gently turns from northeast to northwest trends

on opposite sides of the small Canal Basin, located at the apex of its curvature. Immediately east of the Canal Basin, and unlike the rest of the actively volcanic Central American geologic province, an ~300-km-long, curvilinear, basin-range pair with no active volcanism (Chucunaque–San Blas) traces the northwest-trending segment of the curvature.

The stratigraphy of the isthmus can be separated in two main sequences: (1) an older basement complex consisting of basalt, diabase, and basaltic andesite rocks, interbedded with pelagic sediments (chert and siliceous limestone), intruded by plutonic bodies ranging from granodiorite to gabbro in the San Blas Range (Wörner *et al.*, 2009; Wegner *et al.*, 2011), and (2) a younger overlapping cover sequence composed of sedimentary (mostly clastic and occasional limestone) and volcanoclastic (tuff, agglomerate, and minor basalt) strata. The younger cover sequence rests unconformably on the basement complex in the Canal Basin and the western Chucunaque Basin (Fig. 1).

Radiometric dating in the basement complex (see Fig. 1; Guidice and Recchi, 1969; Kesler *et al.*, 1977; Aspden *et al.*, 1987; Defant *et al.*, 1991a, 1991b; Maury *et al.*, 1995; Speidel *et al.*, 2001; Lissina, 2005; Rooney *et al.*, 2010; Wegner *et al.*, 2011) shows that significant magmatic activity started around 70 Ma, peaking around 50 Ma (Fig. 1, inset). In the Canal Basin and east of it, magmatic activity diminished after 38 Ma, and stopped at ca. 15 Ma, while remaining prolific toward the west (Fig. 1, inset). Late Cretaceous and younger magmatism resulted from north-dipping subduction that is interpreted to have started at 66 Ma along the western edge of the Caribbean plate, defining the time when the Caribbean and Farallon plates became separate kinematic blocks (Pindell and Kennan, 2009). This magmatism continued until at least 40 Ma, as indicated by large volumes of low-K tholeiitic basaltic magmas (Wegner *et al.*, 2011). The spatial distribution of ages delineates two magmatic belts (Lissina, 2005): (1) a latest Cretaceous to Eocene belt, left-laterally displaced more than 200 km (from Azuero Peninsula to San Blas Range, Fig. 1); and (2) a continuous, roughly east-west-trending, Oligocene to Miocene belt with ages younger than 38 Ma (Fig. 1). Left-lateral offset of the older arc took place between 40 and 30 Ma (Lissina, 2005).

Sedimentation in the Canal Basin starts with upper Eocene to Oligocene, chiefly terrigenous, partly subaerial strata (Gatuncillo Formation; Woodring, 1957; Graham *et al.*, 1985; Tripathi and Zachos, 2002), directly overlying a deformed basement complex in angular unconformity (Fig. 2). Upper Eocene strata have also been recognized in the Chucunaque Basin,

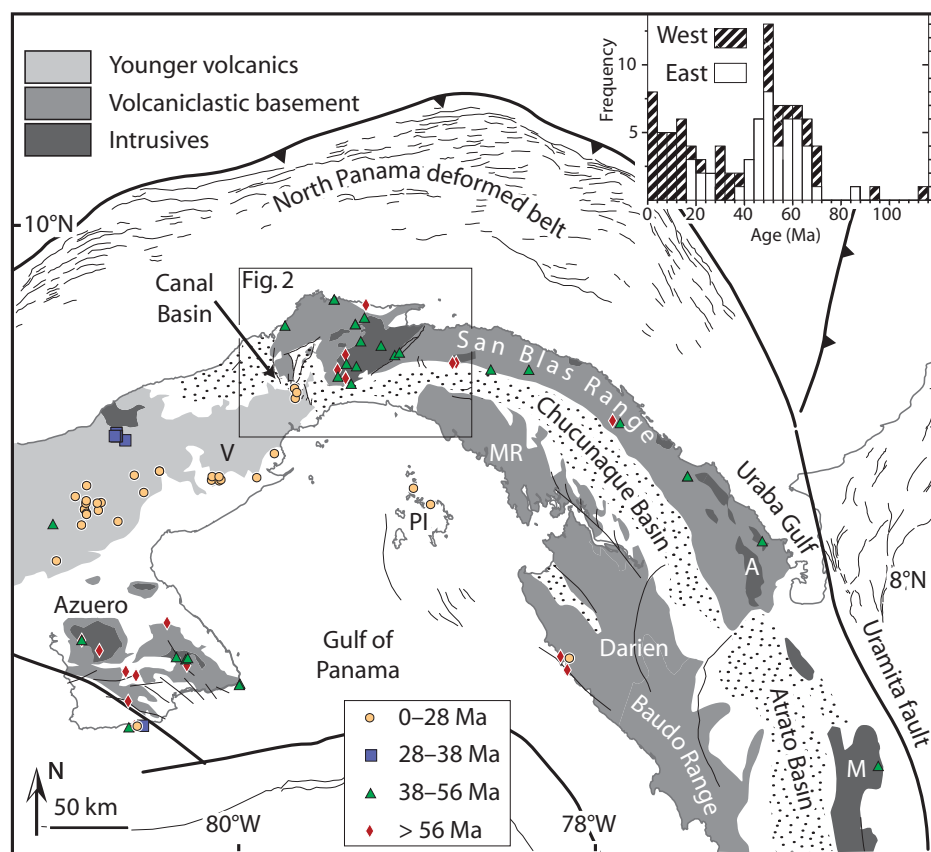


Figure 1. Tectonic setting of the Isthmus of Panama (compiled from: Woodring, 1957; Stewart *et al.*, 1980; Duque-Caro, 1990; Mann and Corrigan, 1990; Silver *et al.*, 1990; Mann and Kolarsky, 1995; Kerr *et al.*, 1997; Coates *et al.*, 2004; Buchs *et al.*, 2010). A—Acandí Batholith; MR—Maje Range; PI—Pearl Islands; M—Mande Batholith; V—El Valle Volcano. Inset shows geochronologic data (compiled from: Guidice and Recchi, 1969; Kesler *et al.*, 1977; Aspden *et al.*, 1987; Defant *et al.*, 1991a, 1991b; Maury *et al.*, 1995; Speidel *et al.*, 2001; Lissina, 2005; Rooney *et al.*, 2010; Wegner *et al.*, 2011), and also includes geochronologic data reported in this study. Histogram shows the same geochronologic compilation separated in two groups: west of the canal in diagonal pattern, and Canal Basin and east of the canal in white.

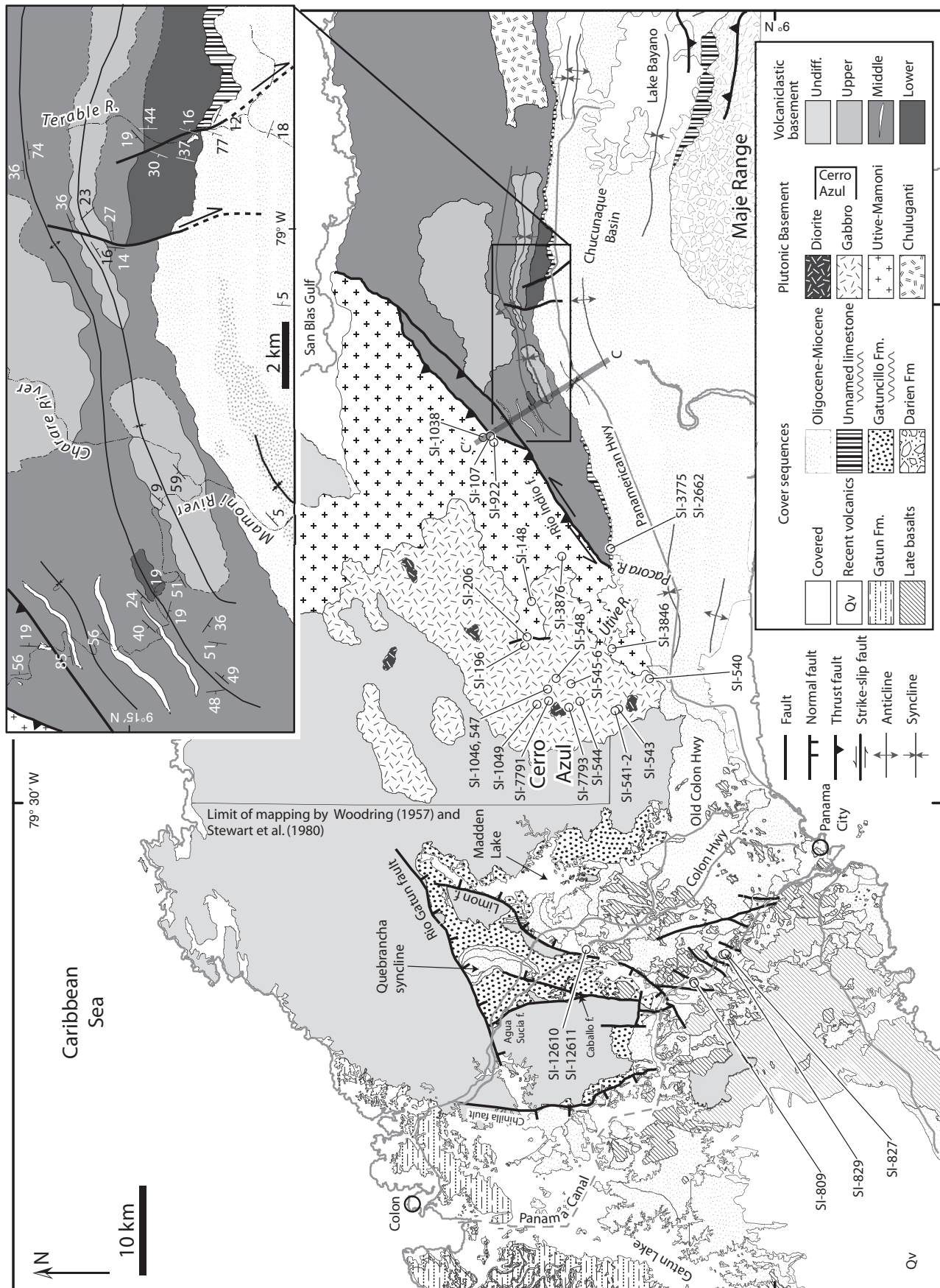


Figure 2. Geologic map of central Panama (from original mapping and compilation from Woodring, 1957; Stewart et al., 1980; Wörner et al., 2009). Note the regional extent of the unconformity separating the basement complex from Upper Eocene to Oligocene strata. Inset shows geologic map between the Mamoní and Terabale Rivers. Dots represent samples referenced in text; see Table 1 for sample summary and coordinates.

where up to 1700 m of limestone, agglomerate, and tuff are continuous eastward near the Colombian border (Shelton, 1952; Terry, 1956; Coates et al., 2004). Upper Eocene conglomeratic, shallow-marine limestone—and locally coal-bearing strata—have also been reported in the Gulf of Panama, the Pearl Islands, and the Azuero Peninsula (Tonosi Formation; Kolarsky and Mann, 1995; Kolarsky et al., 1995).

Oligocene to Miocene sedimentation in the Canal Basin laid a succession of mostly sub-aerial volcanic to volcanoclastic rocks (Bas Obispo and Las Cascadas Formations), which is overlain by a shallow-marine to continental sequence (Culebra and Cucaracha Formations), which in turn is topped by a volcanic and volcanoclastic unit, the Pedro Miguel Formation. These units have been extensively studied on exposures along the Panama Canal (Woodring, 1957; Blacut and Kleinpell, 1969; Stewart et al., 1980; Retallack and Kirby, 2007; Kirby et al., 2008). This early Miocene sedimentary and volcanoclastic succession bears fossils (MacFadden, 2006; MacFadden et al., 2010) that suggest the presence of a peninsula that connected North America to Panama during the early Miocene (Whitmore and Stewart, 1965; Kirby and MacFadden, 2005).

Strata from western Panama to western Colombia contain foraminifera interpreted to record gradual emergence leading to full closure of the isthmus, ending communication between Caribbean and Pacific waters by 3.5 Ma (Coates et al., 2004). From west to east, the lower and middle Miocene Punta Alegre, San Blas Complex, Darien, Pocorna, Clarita, Uva, and Naipipi Formations are interpreted to record bathyal depths, changing to shallower, coarsening-upward sequences in upper middle Miocene strata (Tapaliza, Tuira, Membrillo, Yaviza, and Chucunaque Formations; Coates et al., 2004). Shallowing, coarsening-upward sequences were dated from 14.8 to 12.8 Ma and are interpreted to mark docking of the Panama block to northwestern South America, coeval with the rise and emergence of a volcanic arc recorded in the Gatun Formation of the Canal Basin (Collins et al., 1996; Coates et al., 2004). Easternmost Panama seems to have only emerged by 8.6 Ma, as recorded by coquina limestone and oyster banks in the Yaviza Formation, with sea-level changes breaching a low-elevation isthmus by 6 Ma.

SAMPLING AND ANALYTICAL METHODS SUMMARY

We mapped, sampled, and undertook analytical studies with the goal of refining existing geologic maps and chronology of basement and cover sequences. U/Pb dating was conducted

on magmatic zircons extracted from granitoids and felsic tuffs, and on detrital zircons extracted from lithic sandstone. Magmatic apatites and zircons were separated from granitoids in an elevation profile in central Panama for thermochronological analyses. Calcareous nannoplankton and large foraminifera were analyzed to place biostratigraphic constraints on key stratigraphic horizons in the sedimentary cover sequences.

Stratigraphic Mapping

We conducted geologic mapping covering an area of 845 km² with more than 400 field stations along a dense network of rivers draining the rugged southern flank of the San Blas Range where altitudinal differences of more than 500 m are common. For the western half, we compiled Woodring's (1957) and Stewart et al.'s (1980) geologic maps, complemented with mapping along the new highway transects and Panama Canal cuts, totaling over 2000 field stations. Canal exposures cover a length of 20 km from the Pacific entrance of the canal to the town of Gamboa, with fresh artificial slopes up to 50 m high and up to 500 m wide, due to canal expansion.

We used differentially corrected global positioning system (GPS) units yielding submeter precision to generate geologic maps in the excavation benches of the Canal Basin area. Elsewhere, we conducted conventional geologic mapping using 90 m resolution SRTM (Shuttle Radar Topography Mission) data from the National Aeronautics and Space Administration (NASA) as a topographic base. Stratigraphic columns presented here were measured, sampled, and described using the Jacob staff in sedimentary units, and assembled from the geologic map for the basement complex. Sandstone modal analyses were performed on medium-grained and coarser sandstones, where 300 grains of framework were counted (standard deviation $\pm 5\%$; van der Plas and Tobi, 1965). The Gazzi-Dickinson method was applied to eliminate the problems associated with compositional changes due to grain size (Ingersoll et al., 1984). Carbonate fragments were included in the framework counting; however, they were not considered in the modal calculation of the triangles of Dickinson (1985). Matrix/cement percentages were assessed to assure that samples had less than 30% of matrix/cement and that

the framework counting was statistically significant. Modal analyses tables, as well as sample descriptions are in the GSA Data Repository.¹

U/Pb Geochronology

U-Pb-Th geochronology was conducted at the University of Arizona following procedures established by Valencia et al. (2005), Gehrels et al. (2006), and Gehrels et al. (2008). Zircon crystals were extracted from samples by traditional methods of crushing and grinding, followed by separation with a Wilfley table, heavy liquids, and a Frantz magnetic separator. Samples were processed such that all zircons were retained in the final heavy mineral fraction. Picking of zircon crystals was done on plutonic samples, which in general are characterized by relatively low zircon abundance. A split of zircon grains was selected from the grains available in the detrital samples. Zircons were incorporated into a 2.5 cm diameter epoxy mount together with fragments of Sri Lanka standard zircon. The mounts were sanded down to a depth of $\sim 20\ \mu\text{m}$, polished, and cleaned prior to isotopic analysis.

Zircon crystals were analyzed in a Micro-mass Isoprobe multicollector-inductively coupled plasma-mass spectrometer (ICP-MS) equipped with nine Faraday collectors, an axial Daly collector, and four ion-counting channels (see Appendix for details). In the case of the zircons recovered from plutonic rocks, most of the analyses were done at the zircon tips in order to constrain the late zircon crystallization history (Valencia et al., 2005). In detrital samples, the cores of the grains were analyzed to avoid complex zircon histories (Gehrels et al., 2006). Cathodoluminescence images on selected samples were obtained after U-Pb analysis at the Center for Electron Microscopy and Microanalysis of the University of Idaho in order to review the analytical premise of single growth zircon histories at the tips.

U-Pb zircon crystallization ages (weight averages) were estimated and plotted using Isoplot 3.62 (Ludwig, 2007) and the Arizona Laser-Chron Excel macro age pick program. Reported ages are $^{206}\text{Pb}/^{238}\text{U}$, as they are Cenozoic samples. The uncertainty of the age is determined as the quadratic sum of the weighted mean error plus the total systematic error for the set of analyses. The systematic error, which includes contributions from the standard calibration, age of the calibration standard, composition of

¹GSA Data Repository item 2012073, (1) U/Pb geochronological data table; (2) coordinates for petrographic samples; (3) point counting in granitoids; (4) point counting in arenites; (5) time-temperature paths and track lengths distributions obtained with HeFTy[®] for samples in the Cerro Azul profile; (6) thin section sample descriptions and photographs; (7) compilation of published geochronological ages; and (8) apatite fission-track length results, is available at <http://www.geosociety.org/pubs/ft2012.htm> or by request to editing@geosociety.org.

common Pb, and U decay constants, is $\sim 1\%$ – 2% (2σ). Representative age populations were considered when more than three grains overlapped in age (Gehrels et al., 2006). This statistical assumption relies on the fact that individual grains may sometimes represent Pb loss trajectories.

Apatite Fission Tracks

Apatite concentrates were obtained from crushed and sieved samples of plutonic rocks through standard magnetic and heavy liquid separation techniques. Grains for each sample were mounted in epoxy squares (1.5 cm^2), ground, and polished to an optical finish to expose internal grain surfaces, and subsequently etched for $\sim 20\text{ s}$ in 5.5 M HNO_3 at $\sim 20^\circ\text{C}$. Mount surfaces were cleaned, and suitable crystals were identified and recorded in a mount-specific coordinate system prior mass spectrometry analysis at the Geo-Analytical Laboratory, Washington State University, Pullman, Washington, USA. The laser ablation (LA) ICP-MS method was used for age determinations. LA-ICP-MS measurements of $^{238}\text{U}/^{43}\text{Ca}$ ratios were carried out to obtain the concentration of ^{238}U by focusing the laser on a fixed spot over each dated grain, a procedure known as spot analysis (Donelick et al., 2005). Where possible, fission tracks in ~ 25 – 30 suitable apatite grains were counted for age determinations, while 100 – 130 horizontal confined track lengths were measured per sample. Apatite mounts were irradiated by a ^{252}Cf source in a vacuum to enhance measurability of populations of confined natural tracks (Donelick and Miller, 1991). Fission-track pooled ages were calculated using the modified fission-track age equation proposed by Donelick et al. (2005), which encompasses a MS-zeta calibration method (ζMS). Observed age spread was determined statistically using the chi-square test, which indicates the probability that all grains counted belong to a single population of ages (Galbraith and Laslett, 1993; Galbraith, 2005). A chi-square probability of $<5\%$ is evidence of an asymmetric spread of single-grain ages. Although this criterion is usually applied to the external detector method, here it is used as an assessment of age spread. All ages reported are central pooled ages (Galbraith, 1981, 2005; Galbraith and Laslett, 1993), i.e., weighted-mean ages. We modeled fission-track data with HeFTy[®], which incorporates grain age, track length, and Dpar. The kinetic parameter Dpar is defined as the arithmetic mean diameter of the fission-track etch pit parallel to the crystallographic c axis of the polished and etched surface of the analyzed grain (Ketcham et al., 1999; Ketcham, 2008). Our modeling strategy started with an open-ended model with minimal

constraints. Restrictions were imposed incrementally and directed by the successive modeling results and relevant geologic data, such as stratigraphic age, the sample's pooled apatite fission-track (AFT) age, etc. We used a multi-kinetic annealing approach, which allows for modeling of multiple kinetic apatite populations with Dpar (Ketcham et al., 1999). For the initial general model, we ran 15,000 simulations with a controlled random search technique for each sample. All age and track-length data were modeled as one kinetic population projected to the c axis to effectively remove the problems of anisotropic track-length reduction (Donelick et al., 1999). More details on analytical and modeling procedures can be found in the Appendix.

Zircon and Apatite Helium Dating

All (U-Th)/He analytical procedures were performed at the University of Arizona Radiogenic Helium Laboratory following a protocol based on methods reported for apatite (House et al., 1999, 2000; Farley, 2002) and for zircon (Farley, 2002; Reiners, 2005). When possible, two single zircon and apatite aliquots were selected for analysis. Apatite and zircon crystals were handpicked using a high-power ($180\times$) stereozoom petrographic microscope with cross-polarization, which allows inclusion screening under reflected and transmitted light. The most transparent, inclusion-free, euhedral, nonfractured grains with similar shape and size were selected (average prism width $\sim 80 \pm 10\text{ }\mu\text{m}$, length/width ratios of less than 1.5). Uniform grain size minimizes differences in He diffusion behavior (Farley, 2000; Hourigan et al., 2005).

Sizes >60 – $70\text{ }\mu\text{m}$ require low correction factors for He ages and provide increased accuracy (Farley, 2002). Selected grains were digitally photographed and geometrically characterized by measuring each grain for its prism length (parallel to the c axis) and prism width in at least two different orientations (perpendicular to the c axis). Measurements were used to perform alpha ejection corrections (Ft) (Farley, 2002). Helium isotopic measurements were made by degassing each sample replicate through laser heating and evaluating ^4He by isotope-dilution gas source mass spectrometry. Radiogenic He was analyzed using a fully automated mass spectrometry system consisting of a Nd-YAG laser for total He laser extraction, an all-metal, ultrahigh-vacuum extraction line, a precise volume aliquot system for ^4He standard and ^3He tracer for isotopes, a cryogenic gas purification system, and a Blazers Prisma QMS-200 quadrupole mass spectrometer for measuring $^3\text{He}/^4\text{He}$ ratios. Two single-grain aliquots per sample

were prepared following the standard protocol available at the University of Arizona. Determination of U, Th, and Sm were performed on the same crystals by isotope-dilution ICP-MS on a Thermo Element 2 ICP-MS also at the University of Arizona. Mean (U-Th)/He ages were calculated on the basis of two apatite and zircon replicate analyses. Details on the zircon and apatite He dating procedures are also presented in the Appendix.

RESULTS

In the following section, petrographic sample descriptions are identified with the prefix SI-, and descriptions can be found in GSA Data Repository 6 (see footnote 1). Sample coordinates and a summary of analytical results are presented in Table 1; analytical details can be found in the GSA Data Repository (see footnote 1).

Basement Complex Stratigraphy

The basement of central Panama, described along the southern flank of the San Blas Range (Fig. 1), is composed of three main units well exposed along a coherent, east-west-trending, north-verging, anticline-syncline pair (Fig. 3) intruded by three different plutons. The units from bottom to top are: (1) massive and pillow basalt interlayered with chert and limestone, crosscut by diabase dikes (Terable River; Fig. 2, inset); (2) massive basalt, pillow basalt, diabase, and basaltic dikes and interlayered pelagic sedimentary rocks (upper Mamoni River); and (3) basaltic andesite lava flows and tuff (Charare River). Plutonic rocks ranging in composition from gabbro to granodiorite (Fig. 3A) intrude the basaltic sequences in at least three areas from west to east: Cerro Azul, Mamoni River, and north of Lake Bayano (Fig. 2).

Volcaniclastic Basement Complex

The three field-mappable units within the volcaniclastic basement contain well-defined layers of pillow basalt, lava flows, and chert, which allow definition of the large-scale map structure (Fig. 3C) and arrangement of the stratigraphic order. The lower unit of the volcaniclastic basement, best exposed along the Terable River (Fig. 2, inset), forms the southern flank of a syncline that is cut to the west by discrete north-south faults that locally disrupt bedding planes and stratigraphic relations. The volcanic rocks are predominantly dark-gray diabase (SI-3798), massive basalt, and amygdular pillow basalt (SI-3802). There are rare, lenticular volcanic breccia layers interbedded with the pillow basalt. Discontinuous layers of stratiform chert,

TABLE 1. SAMPLE SUMMARY AND COORDINATES

TABLE 1. SAMPLE LOCATION, AGE, AND LITHOLOGY					
Sample	Long (W)	Location Lat (N)	Age (Ma)	Technique	Lithology
Paleontology					
SI-758	79°40'41.32"	9°04'51.17"	Early Miocene	Calcareous nannofossil	Mudstone
SI-757	79°40'41.28"	9°04'51.09"	Early Miocene	Calcareous nannofossil	Sandstone
SI-759	79°40'41.70"	9°04'50.80"	Early Miocene	Calcareous nannofossil	Mudstone
SI-760	79°40'41.77"	9°04'50.70"	Early Miocene	Calcareous nannofossil	Mudstone
SI-762	79°40'42.32"	9°04'50.53"	Early/middle Miocene	Calcareous nannofossil	Mudstone
SI-3775	79°14'52.64"	9°09'41.88"	Oligocene	Larger foraminifera	Sandstone
SI-2662	79°15'07.38"	9°09'52.26"	Oligocene (?)	Larger foraminifera	Limestone
SI-12611	79°37'51.60"	9°14'03.69"	Oligocene	Larger foraminifera	Sandstone
SI-12610	79°39'23.97"	9°12'10.74"	Oligocene	Larger foraminifera	Fossiliferous sandstone
U/Pb geochronology					
SI-809	79°40'42.47"	9°04'51.49"	19.3 ± 0.4	Magmatic zircon	Ash tuff
SI-8023	79°40'48.61"	9°04'58.93"	—	—	Ash tuff*
SI-8022	79°40'48.27"	9°04'58.19"	—	—	Ash tuff*
SI-540	79°22'32.35"	9°07'38.56"	54.1 ± 1.2	Magmatic zircon	Diorite
SI-542	79°24'24.43"	9°09'31.42"	58.7 ± 1.4	Magmatic zircon	Diorite
SI-543	79°24'23.34"	9°09'32.41"	58.5 ± 1.3	Magmatic zircon	Diorite
SI-107	79°07'58.34"	9°17'06.33"	39.4 ± 0.8	Magmatic zircon	Granodiorite
SI-1038	79°07'58.80"	9°17'24.30"	49.7 ± 1.0	Magmatic zircon	Granodiorite
SI-1049	79°24'05.40"	9°14'17.40"	54.7 ± 1.2	Magmatic zircon	Diorite
SI-827	79°39'14.20"	9°02'52.75"	—	Detrital zircon	Sandstone
SI-829	79°39'07.95"	9°02'54.24"	—	Detrital zircon	Sandstone
SI-7683	79°40'57.65"	9°14'34.97"	—	—	Sandstone*
SI-8542	79°41'14.89"	9°16'05.26"	—	—	Sandstone*
Thermochronology					
SI-196	79°20'24.95"	9°15'24.96"	35.8 ± 2.4	Apatite fission track	Granodiorite
SI-206	79°19'52.32"	9°15'16.51"	45.4 ± 3.6	Apatite fission track	Granodiorite
SI-148	79°17'42.92"	9°14'58.35"	45.4 ± 4.2	Apatite fission track	Granodiorite
SI-3846	79°20'36.23"	9°10'0.00"	46.3 ± 2.1	Apatite fission track	Tonalite
SI-922	79°08'07.29"	9°17'17.39"	42.6 ± 4.8	Apatite fission track	Tonalite
SI-1046	79°23'02.40"	9°14'0.39"	50.1 ± 9.4	Apatite fission track	Microgabbro
SI-3876	79°15'02.69"	9°13'05.99"	45.7 ± 3.7	Apatite fission track	Granodiorite
SI-7788	79°24'20.04"	9°12'05.15"	85.5 ± 30.4	Apatite fission track	Diorite
SI-7791	79°23'44.93"	9°13'58.92"	47.3 ± 3.6	Apatite fission track	Diorite
SI-7793	79°24'08.80"	9°12'41.53"	44.8 ± 8.2	Apatite fission track	Diorite
SI-540	79°22'32.35"	9°07'38.56"	11.4 ± 0.5	Apatite U-Th/He	Diorite
			6.2 ± 1.6	Apatite U-Th/He	
			41.4 ± 2.0	Zircon U-Th/He	
			50.9 ± 1.6	Zircon U-Th/He	
SI-541	79°24'24.35"	9°09'31.60"	12.0 ± 7.4	Apatite U-Th/He	Granodiorite
			50.1 ± 1.8	Zircon U-Th/He	
			44.2 ± 1.6	Zircon U-Th/He	
SI-543	79°24'23.34"	9°09'32.41"	42.8 ± 1.5	Zircon U-Th/He	Diorite
			40.1 ± 1.5	Zircon U-Th/He	
SI-544	79°23'56.78"	9°11'46.18"	47.7 ± 1.9	Zircon U-Th/He	Diorite
			43.9 ± 1.6	Zircon U-Th/He	
SI-545	79°22'52.35"	9°12'19.33"	12.7 ± 0.8	Apatite U-Th/He	Granodiorite
			40.2 ± 1.5	Zircon U-Th/He	
SI-546	79°22'51.16"	9°12'17.55"	41.3 ± 1.6	Zircon U-Th/He	Diorite
			48.9 ± 1.8	Zircon U-Th/He	
SI-547	79°22'53.44"	9°13'42.20"	48.8 ± 1.8	Zircon U-Th/He	Diorite
			51.0 ± 1.8	Zircon U-Th/He	
SI-548	79°22'31.09"	9°13'11.45"	23.3 ± 0.8	Apatite U-Th/He	Diorite
			12.6 ± 1.2	Apatite U-Th/He	
			50.6 ± 1.9	Zircon U-Th/He	
*Barren of zircons.					

*Barren of zircons.

tuffaceous siltstone, and micritic limestone are interbedded with the basalt. The sedimentary layers are lenticular and are up to 15 m thick. Very fine-grained basaltic and andesitic dikes crosscut the volcanic and marine sediments. The dikes are pilotaxitic and contain clinopyroxene crystals and lath-shaped, randomly oriented plagioclase crystals. The vesicles are filled with calcite and pumpellyite (SI-3801).

Overlying the lower volcanoclastic unit, and well exposed on both flanks of an anticline along the Mamoni River (Fig. 2, inset), the middle volcanoclastic unit (Fig. 3) consists of massive basalt

and andesite, pillow basalt (Fig. 3B; SI-2685), amygdular basalt, porphyritic andesite, and diabase sills and dikes. Chert beds (SI-3783, SI-3757) and tuffaceous siltstone that are up to 2 m thick and continuous for >1 km are interbedded with the volcanic layers. Fine-grained basaltic and rare medium-grained dioritic dikes (SI-3750) crosscut the sequence of volcanics and marine sediments. The groundmass in the volcanic rocks consists of lath-shaped plagioclase and subhedral clinopyroxene grains with significant epidote alteration (SI-2658, SI-2691, SI-2682). There are two dominant phenocryst

assemblages. Mostly, the basalts and the andesite have plagioclase, clinopyroxene, and rare orthopyroxene phenocrysts. However, some of the basalts contain only plagioclase phenocrysts. In the amygdular basalts, the vesicles are filled with calcite and silica.

The upper unit of the volcanoclastic basement is exposed in the core of a syncline along the Charare and the Mamoni Rivers (Fig. 2, inset), forming resistant ridges, cliffs, and narrow, deep canyons. This unit consists of lavas and volcanic breccia (Fig. 3). The lavas are stratiform, massive andesitic lavas with centimeter-scale

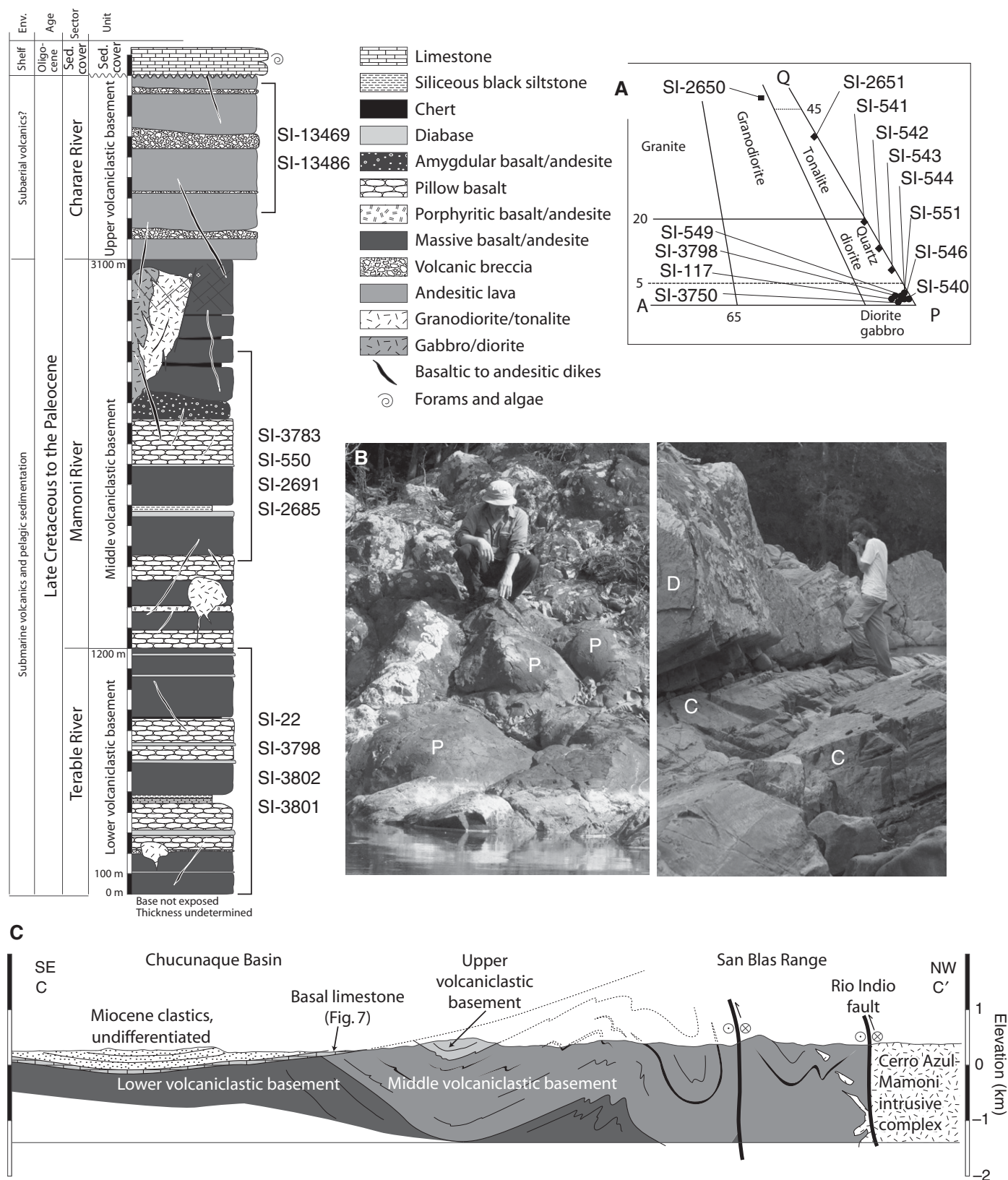


Figure 3. Schematic stratigraphic column of the basement complex assembled from observations along the Terable, Mamoni, and Charare Rivers (Fig. 2, inset). (A) Modal analyses of granitoid rocks; (B) field photographs of south-dipping pillow basalts (P) and a sequence of chert (C) and a massive, tabular diabase (D) in the Mamoni River; and (C) cross section along the Mamoni River. See Figure 2 for location and GSA Data Repository (see text footnote 1) for sample descriptions and coordinates.

layering (SI-13468). Interbedded breccias with similar composition, probably representing brecciated top flows or bases of lava flows, are up to 15 m thick. The breccias consist of angular to subrounded clasts of andesitic lava and a matrix of andesitic lava that is commonly more altered than the clasts. Diabase dikes and sills intrude these layers (SI-13469).

The age of the volcanoclastic basement is Late Cretaceous to Eocene. Direct ages between 65.7 ± 4 and 41.5 ± 2 Ma have been obtained on the undifferentiated belt of mafic volcanic and volcanoclastic rocks (green triangles in westernmost tip of San Blas Range, Fig. 1) by Ar/Ar techniques (Wegner et al., 2011), while basaltic volcanic arc rocks and interbedded pelagic sediments of southern Costa Rica and Azuero Peninsula (Fig. 1) have been dated as upper Campanian (Buchs et al., 2010). On the western half of the geologic map (Fig. 2), the volcanoclastic basement remains undifferentiated, partially because of a more intense deformation fabric, but also because of limited access to this region.

Igneous Rocks Intrusive into the Basement Complex

Three main plutons intrude the volcanoclastic basement east of the Canal Basin (Fig. 2): (1) a two-pyroxene gabbro to diorite exposed in the Cerro Azul area; (2) a predominantly clinopyroxene quartz diorite well exposed ~30 km to the east of Cerro Azul, near the central part of the geologic map (Utive-Mamoni; Fig. 2); and (3) a granodiorite well exposed in the eastern edge of the geologic map (Chuluganti; Fig. 2). We focused our studies in the first two. The third one was dated by Wegner et al. (2011) using Ar/Ar dating on amphibole, yielding latest Cretaceous ages (ca. 66 Ma). All three of these plutons are massive, with only local and poorly defined magmatic foliation. Metamorphic aureoles defined by radiating aggregates of fibrous actinolite in basaltic basement rocks are variably found within ~1 km of the intrusive rocks.

The first pluton, a two-pyroxene gabbro to diorite exposed in Cerro Azul (Fig. 2), is medium-grained, massive, and equigranular with cumulate textures, defined by an interstitial poikilitic pyroxene surrounding plagioclase grains. Pyroxenes show rims that are altered to hornblende (SI-551, SI-552, SI-544, SI-546, SI-549, SI-540). The second pluton is a clinopyroxene quartz diorite (SI-541, SI-542, SI-543), hornblende tonalite (SI-2651), hornblende diorite (SI-117), and granite, which are all exposed along the southern flank of the San Blas Range (upper Mamoni, Pacora, and Utive Rivers; Fig. 2, inset). Mafic magmatic enclaves that range from subangular to rounded contain-

ing clinopyroxene + plagioclase \pm olivine are common in the Utive River (Fig. 2) area, as well as equigranular, fine- to medium-grained leucogranodioritic dikes and synintrusional, fine-grained mafic dikes that crosscut all the intrusive units (SI-550, SI-552). The quartz diorite is medium grained and inequigranular, with subhedral clinopyroxene commonly altered to green hornblende and rare orthopyroxene. Hornblende tonalites, granodiorites (SI-2650), and granites are medium grained and equigranular. Gabbroic xenoliths within the quartz diorite and apophyses of quartz diorite within the gabbro unit of Cerro Azul indicate that the contact between these units is intrusive and the gabbro is older. Brittle, north-south, strike-slip faults locally overprint the contact where grain comminution takes place, and shears contain epidote and chlorite.

In total, six granitoid samples (Fig. 4; Table 1) were processed to separate and date zircons in the basement complex of central Panama. All the analyzed zircons are fragmentary or have a needle morphology, which is typical of more mafic rocks (Corfu et al., 2003; see Fig. 4). U/Th ratios < 12 (GSA Data Repository [see footnote 1]) are also a characteristic feature of magmatic zircons (Rubatto, 2002). Four gabbroic rocks from Cerro Azul and the two tonalite to quartzdiorite samples from Mamoni yield Paleocene-Eocene ages of 58–54 Ma and 49–39 Ma, respectively.

Fission-track and (U-Th)/He low-temperature thermochronology was conducted on 16 plutonic samples collected from topographic profiles at the deeply incised Cerro Azul Range, where ~1 km differences in elevation are present in < 10 km radius (Fig. 2). Together, these data represent the first low-temperature thermochronology study in the Isthmus of Panama.

Apatite fission-track (AFT) dating on 10 plutonic samples yielded ages between 50 Ma and 36 Ma (mean ca. 45 Ma), and analyses display excellent reproducibility (Tables 2 and 3). All AFT ages are younger than zircon U-Pb ages obtained from the Cerro Azul intrusives (ca. 54–58 Ma; Fig. 4). Only sample SI-7788 yielded a poorly defined age of 85.5 ± 30.4 Ma (Table 1; only four optically cloudy apatite grains with much crystallographic heterogeneity and low track density could be analyzed for this sample), and it is therefore excluded from further discussion. The propagated 2σ analytical error on apatite fission-track analysis by LA-ICP-MS is estimated at ~6% (Donelick et al., 2005).

Chi-squared values calculated for our samples (Table 3) in general validate our data set. For instance, the ages for sample SI-196 show chi-squared probability of +0.81; this indicates a chi-squared value of 81%, i.e., a strong pass. Similar results were obtained for samples

SI-206, SI-148, SI-1046, SI-922, and SI-7793. On the other hand, the value for sample SI-3876 is 2.62% and fails just barely. Igneous samples, and even standards at times, can fail the chi-squared test and still produce geologically meaningful and accurate data (e.g., O'Sullivan and Parrish, 1995). We further examined the validity of our AFT ages by looking at age versus elevation and age versus mean track-length plots (Figs. 5 and 6). Age-elevation relationships for AFT data at 2σ exhibit virtually concordant ages between 47 and 42 Ma and a moderate positive correlation ($R^2 = 0.3$, $m = 0.07$ km/m.y.; Fig. 5A). Track-length distributions throughout the vertical profile show typical unimodal symmetric patterns clustering around a value of 14.6 μ m, with small track-length standard deviations averaging 1.2 μ m (Table 2; Fig. 5B), implying rapid cooling through the partial annealing zone (PAZ). A plot of age versus mean track length shows a notable positive correlation (Fig. 6) consistent with a relatively simple cooling history, whereby none of the samples spent significant intervals at temperatures where partial annealing occurs, i.e., 60–90 °C. Fission-track ages together with long mean track length indicate that virtually all of the samples record a simple episode of cooling between ca. 42 and 47 Ma, with minimal subsequent annealing. Thermal models undertaken in our study corroborate this finding.

Time-temperature paths were derived for AFT data (Fig. 5B) using the software HeFTy® (Ketcham, 2008). Such models display a marked cooling episode taking place between 47 and 42 Ma. The zircon (U-Th)/He data set also exhibits a clustered nature, in which ages vary from ca. 49 to 41 Ma, with most ages close to 46 Ma, concordant with AFT ages in the same vertical profile (Table 4). A weak positive correlation characterizes this data set ($R^2 = 0.08$). Apatite (U-Th)/He ages vary from ca. 12 to 9 Ma over an elevation difference of ~800 m and exhibit a positive correlation ($R^2 = 0.9$, $m = 0.2$ km/m.y.). Some of the helium ages show large age variations (SI-540, SI-548), which are probably related to the presence of mineral inclusions not detected during grain picking (Fitzgerald et al., 2006).

Measurements of the Dpar parameter between 1.6 and 2.9 μ m indicate that apatite composition for this plutonic suite is possibly variable between recognized thresholds of Dpar values at ~Dpar = 1.75 μ m. Apatites with Dpar < 1.75 μ m are typical near-end-member calcian-fluorapatite apatites, which can, in general, be considered fast annealing. On the other hand, apatites with Dpar > 1.75 μ m regularly, but not always, anneal more slowly than their low Dpar counterparts (Carlson et al., 1999; Donelick et al., 2005). Differential annealing potentially

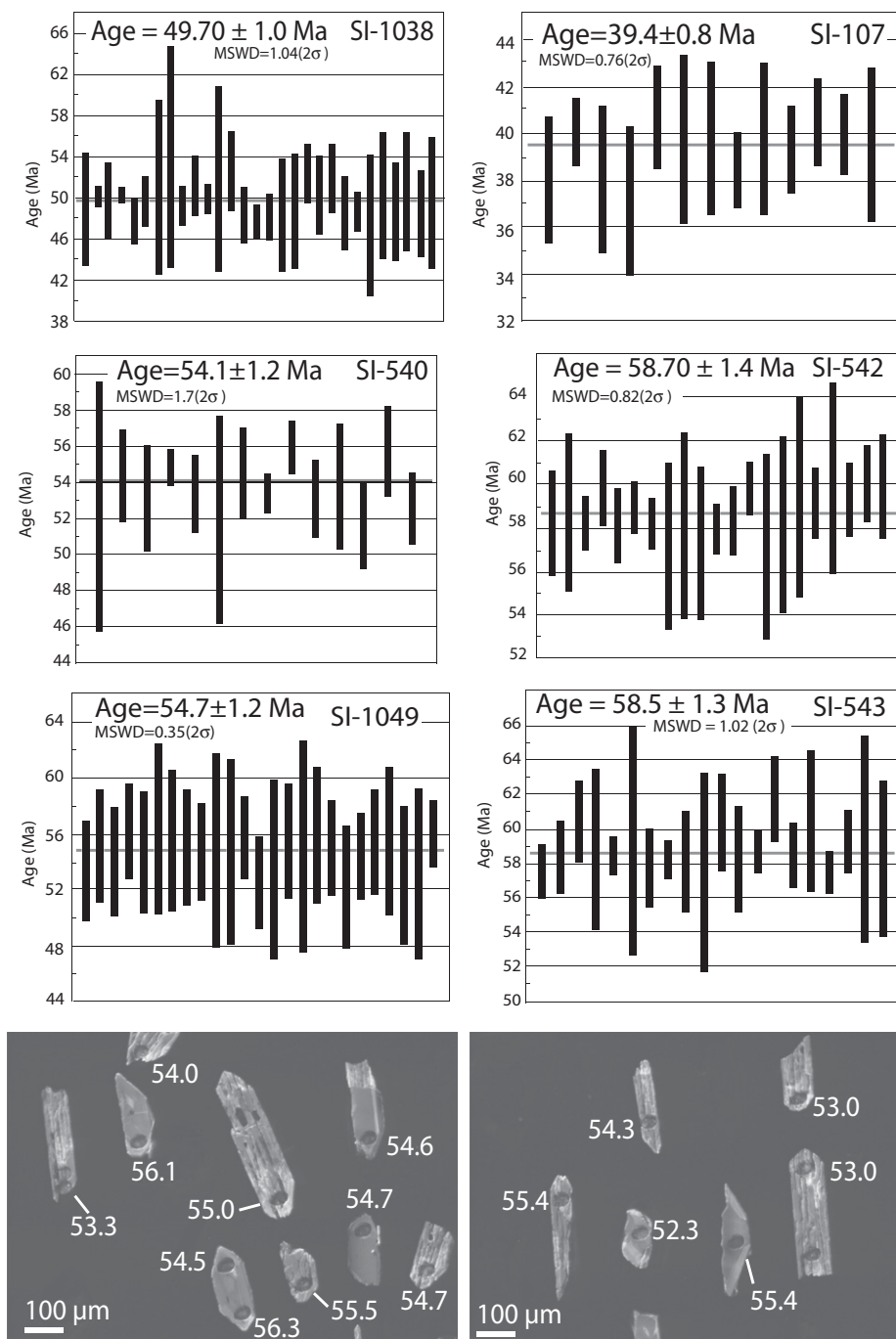


Figure 4. $^{238}\text{U}/^{206}\text{Pb}$ weighted average age plots of zircons extracted from granitoids in central Panama. Below: Cathodoluminescence images of sample SI-1049 showing an example of the location of magmatic zircon tip analyses. MSWD—mean square weight deviation. See Table 1 for sample summary and coordinates and GSA Data Repository for full analytical tables (see text footnote 1).

resulting from such compositional variations may lead to the apparent fission-track age spread of single grains found in some granitic samples, as has been reported elsewhere (O'Sullivan and Parrish, 1995; Restrepo-Moreno et al., 2009). A meaningful correlation between fission-track

age and Dpar was not found in this study, which suggests that any variation of single-grain ages is related to compositional gradients ($R^2 = 0.14$ when the apparently offset value of 35.8 Ma [SI-196] is included and $R^2 = 0.0002$ when the same value is excluded). The distribution of

the data in age-elevation relationships ($R^2 = 0.2$ and concordance with zircon He ages) as well as a potential correlation in age versus track-length diagrams suggest that the ages are not only accurate but are geologically meaningful.

Cover Sequences Stratigraphy

We measured surface stratigraphic sections in the Canal Basin and in the westernmost extension of the Chucunaque Basin (Fig. 1), separating detrital and magmatic zircons for provenance analyses and analyzing calcareous nannoplankton and larger foraminifera for age dating (Table 1).

Eocene to Oligocene Basal Sequences

Upper Eocene to Oligocene strata rest unconformably on the basement complex. From east to west (Fig. 2), these strata directly onlap: (1) the middle and lower parts of the volcanoclastic basement complex; (2) the igneous rocks intrusive into the basement complex; and (3) the undifferentiated part of the volcanoclastic basement complex near the Canal Basin. There are no instances of younger strata (e.g., Miocene strata) resting unconformably on either basement complex or upper Eocene to Oligocene strata (Fig. 2). The map pattern of this unconformity, and the age of the strata immediately above it have been well established by earlier workers (Cole, 1949, 1953; Woodring, 1957; Jenkins, 1964; Stewart et al., 1980; Tripathi and Zachos, 2002) in the western part of the geologic map (Fig. 2). The lowermost strata above the unconformity in the eastern part of the geologic map commonly contain well-preserved, conspicuous larger foraminifera in packstone, grainstone, and wackestone limestone useful for age dating.

The Gatuncillo Formation and other basal units (unnamed limestone of Fig. 2) are the first sediments accumulated on the deformed basement complex where we obtained late Paleocene to Eocene crystallization ages (Fig. 4) and Lutetian cooling ages (Fig. 5). Therefore, the ages of these units bracket the time between the end of deformation-erosion and the beginning of postorogenic sedimentation. The Gatuncillo Formation is a 150–800-m-thick unit that has been described as a mostly muddy unit in the Quebrancha syncline (Fig. 2), and more sandy and conglomeratic in the rest of central Panama, with gritty sandstone and conglomerate with much carbonaceous material and minor limestone (Woodring, 1957). In the Quebrancha syncline (Fig. 2), the Gatuncillo Formation contains coarse detrital material near its base, with minor algal and

TABLE 2. APATITE FISSION-TRACK (FT) SUMMARY: APATITE FISSION-TRACK AGE, TRACK LENGTH, AND Dpar DATA (FISSION-TRACK AGE ERRORS ARE 2σ)

Sample	Grains	Dpar (μm)	Pooled FT age (Ma $\pm 2\sigma$)	Tracks	MTL \pm SE (μm)	TL SD (μm)
Durango-D 31.4 Ma		1.87		138	14.59 \pm 0.08	0.98
Fish Canyon Tuff-D 27.8 Ma		2.36		130	15.01 \pm 0.09	1.02
Age standard Durango	492	1.52	31.4 \pm 1.6			
SI-3846	39	1.92	46.3 \pm 4.2	128	14.58 \pm 0.09	1.02
SI-3876	34	2.35	45.7 \pm 7.4	127	14.83 \pm 0.09	1.04
SI-196	34	1.85	35.8 \pm 4.8	181	14.15 \pm 0.11	1.49
SI-206	37	2.09	45.4 \pm 7.2	130	14.88 \pm 0.09	1.02
SI-148	31	2.28	45.4 \pm 8.4	131	14.69 \pm 0.11	1.23
SI-1046	9	2.45	50.1 \pm 18.8	7	14.17 \pm 0.53	1.3
SI-922	32	2.79	42.6 \pm 9.6	93	14.44 \pm 0.18	1.74
SI-7788	4	2.74	85.5 \pm 60.8	4	14.39 \pm 0.85	1.46
SI-7791	23	3.45	47.3 \pm 7.2	44	14.90 \pm 0.14	0.9
SI-7793	13	2.66	44.8 \pm 16.4	28	14.83 \pm 0.19	0.97
Average values		2.37	48.89		14.59	1.22

Abbreviations: Dpar—arithmetic mean diameter of the fission-track etch pit parallel to the crystallographic *c* axis of the polished and etched surface of the analyzed grain; MTL—mean track length; SE—standard error; TL SD—track length standard deviation.

foraminiferal limestone, and occasional coral fragments, where we collected larger foraminifera samples for age dating.

Lepidocyclina canellei of Oligocene age is a common form in the Gatuncillo limestone (SI-12610, SI-12611, Fig. 2). This foraminifera has hexagonal equatorial chambers; thick-walled embryo with straight wall separating protoconch and deutoconch; and large, open, thin-walled lateral chambers. In the same area, *Lepidocyclina* grainstones contain nephrolepidine to eulepidine *Lepidocyclina* (*Lepidocyclina vaughani* or *Lepidocyclina undosa*) and *Lepidocyclina canellei* with *Nummulites* sp., also of Oligocene age. Upper Eocene Gatuncillo Formation strata (with *Asterocyclina* sp.) are found across the Rio Limon fault (Fig. 2). This is consistent with taxa and ages reported by Woodring (1957). Two samples from coarse- and fine-grained lithic sandstone from Gatun-

cillo Formation yielded no detrital zircons (SI-7683 and SI-8542, Table 1).

Further east (Fig. 2, inset), foraminiferal and red algal wackestone (SI-3800, SI-3775, SI-3774, SI-3772) rest directly on volcanoclastic basement rocks with a marked angular unconformity (Fig. 7). This discontinuous, but regional calcareous unit ("Unnamed limestone" in Fig. 2) contains poorly preserved *Lepidocyclina* sp. and *Nummulites* sp. (SI-3775 and SI-2662, Table 1). The lepidocyclinid is isolepidine with thick embryonic chamber walls. One view of equatorial chambers seems to be hexagonal. Both features suggest *L. canellei*. Siliciclastic/volcanoclastic sediments with interbedded, *Lepidocyclina*-rich beds/coquinas, yielded *Heterostegina* sp., and *Lepidocyclina* (*Nephrolepidina*) *vaughani*, a nephrolepidine form with strongly rhomboid (diamond-shaped) equatorial chambers of Oligocene age. Also present are *Lepi-*

docyclina yurnagunensis and *Lepidocyclina* (*Lepidocyclina*) *canellei*, all Oligocene markers. Above this calcareous unit, a series of tuffaceous sandstones (SI-2676), and fossiliferous mudstone (SI-2674, SI-21) crop out along the northern border of the Chucunaque Basin.

Late Oligocene to Miocene Canal Basin

In the Canal Basin, the volcanic Bas Obispo Formation, a hard, crudely bedded, welded agglomerate, interfingers with the Bohio Formation, a coarse, boulder conglomerate in the southern part of the Gatun Lake (Woodring, 1957). The Bas Obispo and Bohio Formations are overlain by layered tuff and tuffaceous sediments of the Las Cascadas Formation, a unit that grades laterally to the east and northeast into a tuffaceous shallow-marine, heterogeneous sequence included in the Caimito Formation (Woodring, 1957). In the central part of the Canal Basin, the Culebra Formation rests conformably on Las Cascadas Formation, and may be attributable to the same marine transgression recorded by Caimito strata. The volcanic Pedro Miguel Formation followed the accumulation of continental paleosols of the Cucaracha Formation. The age of the Bas Obispo Formation is constrained by a whole-rock $^{40}\text{Ar}/^{39}\text{Ar}$ date obtained southeast of the canal (25.37 ± 0.13 Ma; Rooney et al., 2010), on an andesite body intruding a mafic agglomerate very similar lithologically, and probably correlative to, the agglomerate we sampled in the Canal Basin.

The overlying Las Cascadas Formation is a 390-m-thick volcano-sedimentary succession, characteristically clastic toward the top and more volcanic toward the bottom, within which crude volcanic to sedimentary cycles can be recognized (Fig. 8). These cycles, 30 m-thick, start with black vitric lava or gray welded agglomerate with andesite and basalt fragments,

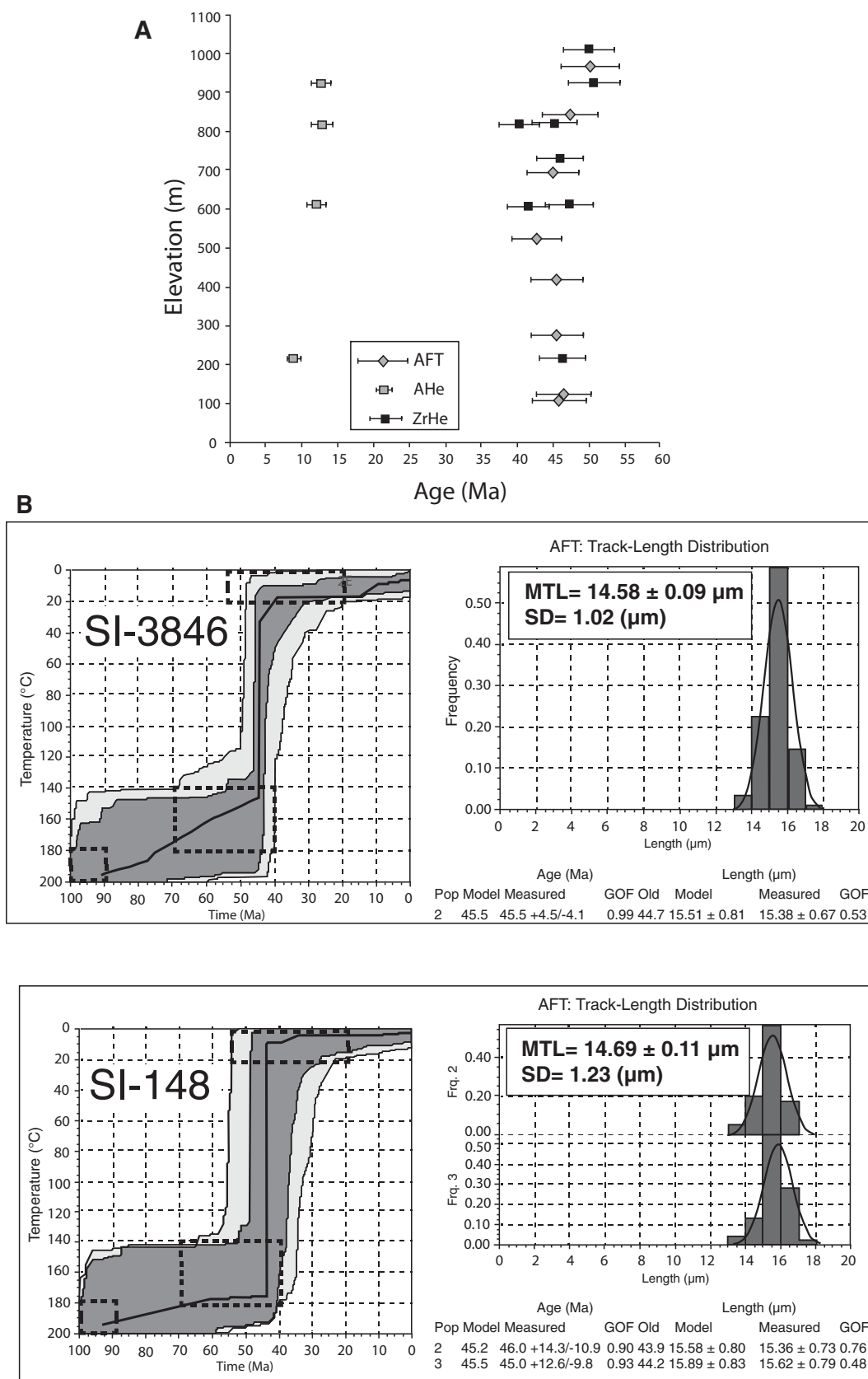
TABLE 3. APATITE FISSION-TRACK LA-ICP-MS DATING RESULTS AND SUMMARY OF THE APATITE FISSION-TRACK POOLED AGES, FOR ALL APATITE GRAINS COMBINED*

Sample	Grains	Dpar (μm)	N_s (tracks)	Area analyzed (cm^2)	$\Sigma(P\Omega)$ (cm^2)	$1\sigma \Sigma(P\Omega)$ (cm^2)	ξ_{MS}	$1\sigma \xi_{\text{MS}}$	^{43}Ca (apatite)	^{238}U bkg:sig (dmnls)	Q (dmnls)	χ^2	P (χ^2)	Pooled fission-track age (Ma $\pm 2\sigma$)
Durango apatite age standard														
DR-06	492	1.52	3091	2.27E-02	7.117E-04	1.335E-06	14.5149	0.2625	2.565E-02	2.166E-03	0.9665			31.4 \pm 1.6
Samples														
SI-3846	39	1.92	592	7.92E-04	8.41E-05	4.89E-07	13.201	0.2704	1.78E-02	4.62E-03	0.000	124.4	0.00	46.3 \pm 4.2
SI-3876	34	2.35	166	5.83E-04	2.40E-05	2.17E-07	13.2261	0.274	1.57E-02	2.97E-03	0.026	50	0.03	45.7 \pm 7.4
SI-196	34	1.85	235	5.65E-04	4.64E-05	2.94E-07	14.1728	0.2711	1.70E-02	9.20E-04	0.803	26	0.81	35.8 \pm 4.8
SI-206	37	2.09	175	6.92E-04	2.55E-05	1.70E-07	13.2513	0.2776	2.14E-02	4.11E-03	0.067	49.4	0.07	45.4 \pm 7.2
SI-148	31	2.28	124	6.68E-04	1.81E-05	1.62E-07	13.2764	0.2812	1.60E-02	3.21E-03	0.919	19.9	0.92	45.4 \pm 8.4
SI-1046	9	2.45	29	1.33E-04	4.10E-06	5.85E-08	14.2088	0.272	2.10E-02	3.70E-01	0.890	3.6	0.89	50.1 \pm 18.8
SI-922	32	2.79	82	4.05E-04	1.37E-05	9.46E-08	14.2448	0.2728	1.77E-02	1.51E-03	0.849	23	0.85	42.6 \pm 9.6
SI-7788	4	2.74	8	4.61E-05	6.18E-07	1.86E-08	13.2984	0.2844	1.24E-02	4.77E-02	0.000	78.8	0.00	85.5 \pm 60.8
SI-7791	23	3.45	197	3.93E-04	2.77E-05	3.18E-07	13.3336	0.2895	1.76E-02	1.19E-03	0.000	135	0.00	47.3 \pm 7.2
SI-7793	13	2.66	31	1.97E-04	4.61E-06	9.32E-08	13.3726	0.2951	1.65E-02	2.81E-03	0.964	4.8	0.96	44.8 \pm 16.4

Note: LA-ICP-MS is laser ablation-inductively coupled plasma-mass spectrometry. Abbreviations: bkg sig—background signal; dmnls—dimensionless.

*Age errors are 2σ (with raw χ^2).

Figure 5. Thermochronology data: (A) Age-elevation relationship for apatite fission-track (AFT) and helium low-temperature thermochronology in apatite (AHe) and zircon (ZrHe) in Cerro Azul. Error bars shown at 2σ . (B) Shaded areas in the temperature-time ($T-t$). Outer, light gray includes acceptable fits; the inner, dark gray contains good fits; thick black line indicates best-fit model (Ketcham, 2005). The track-length distribution plots display a graphic comparison between measured (histogram) and predicted (thin envelope line) values. Boxes below the track-length distributions show fit of the models compared for age and mean track lengths (MTL); such data includes: modeled and measured ages, goodness of fit (GOF) for ages and for MTL. MTL and MTL standard deviation is also included in the box within the histogram diagrams. Time-temperature paths modeled with HeFTy[®] from AFT data are best constrained within the boundaries of the PAZ, i.e., ~60–120 °C. See Table 1 for sample coordinates, Tables 2 and 3, and GSA Data Repository for time-temperatures paths and track-length distributions of all samples (see text footnote 1).



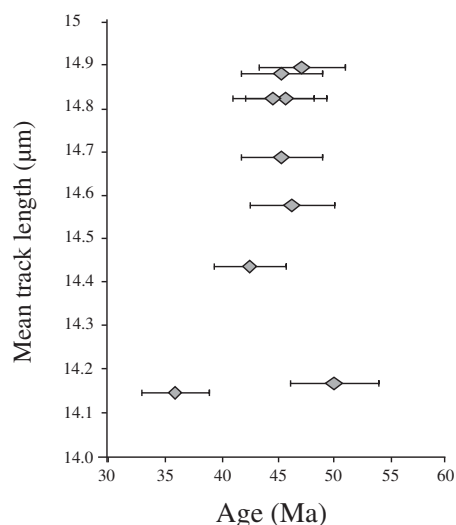


Figure 6. Plot of apatite fission-track age versus mean track length for the Cerro Azul samples. Error bars are plotted at 2σ . See Table 1 for sample coordinates, Tables 2 and 3, and GSA Data Repository for time-temperatures paths and track-length distributions of all samples (see text footnote 1).

commonly covered by cream-colored pumice layers, grading into light-colored lapilli tuff and white ash tuff, and finally to purple ash tuff. The varicolored ash tuff is commonly topped by lenticular bodies of conglomeratic sandstone and purple and green mudstone, where well-preserved terrestrial vertebrate fossil remains have been found. The Las Cascadas Formation is of late Oligocene age, as it overlies the Bas Obispo Formation and underlies the early Miocene Culebra Formation (its base is dated at ca. 23 Ma; Kirby et al., 2008); the upper contact is a sharp (see following), slightly angular, unconformity. Two samples from a felsic, light-colored tuff in Las Cascadas Formation yielded no magmatic zircons (SI-8023 and SI-8022, Table 1).

The Culebra Formation (*sensu* Kirby et al., 2008) conformably underlies the Cucaracha Formation; the base of the Cucaracha Formation is marked by a thick, pebble conglomerate (Fig. 8). The Culebra Formation records shallow-marine siliciclastic sedimentation, with mostly black mudstone, and interbedded tuff beds and calcareous strata. The sandy fraction of this unit is calcite-cemented lithic arenite (Fig. 8A; SI-266, SI-521, SI-663, SI-664, SI-666, SI-965); the framework is made of bioclasts, with lesser amount of lithics, mostly chert, lithic tuff, and basalt fragments. Few plutonic lithics were identified, while detrital glauconite was identified in most samples. Quartz content decreases upward, and the lithic content decreases downward. The

Sample name	Mass (μg)	U (ppm)	Th (ppm)	Sm (ppm)	^4He (nmol/g)	FT	Age (Ma)	Error (Ma, 2σ)	Weighted age (Ma)	Error (Ma, 2σ)	MSWD
Apatite											
SI-540a	2.46	22	3	167	0.97	0.68	11.4	0.5	10.89	0.49	3.6
SI-540b	1.14	7	13	86	0.22	0.64	6.2	1.6			
SI-541a	1.83	0	3	30	0.05	0.67	12.0	7.4			
SI-545a	3.88	7	28	139	0.67	0.73	12.7	0.8			
SI-548a	2.70	11	47	519	1.96	0.70	23.3	0.8	nd	nd	nd
SI-548a	18.18	1	3	31	0.09	0.85	12.6	1.2			
Zircon											
SI-540a	2.63	36	16	—	6.37	0.72	41.4	2.0	nd	nd	nd
SI-540b	5.00	313	429	—	86.20	0.76	50.9	1.6			
SI-541a	4.56	140	99	—	33.52	0.76	50.1	1.8	46.7	1.2	25
SI-541b	3.91	319	223	—	65.73	0.74	44.2	1.6			
SI-543a	6.81	284	218	—	61.52	0.79	42.8	1.5	41.5	1.1	6.6
SI-543b	4.23	195	133	—	36.88	0.75	40.1	1.5			
SI-544a	4.05	91	67	—	19.72	0.72	47.7	1.9	54.5	1.2	9.6
SI-544b	2.33	66	64	—	13.04	0.68	43.9	1.6			
SI-545a	5.41	271	150	—	50.93	0.76	40.2	1.5			
SI-546a	3.50	129	66	—	23.92	0.74	41.3	1.6	44.6	1.2	40
SI-546b	36.74	248	166	—	66.60	0.88	48.9	1.8			
SI-547a	0.92	799	420	—	146.58	0.62	48.8	1.8	49.8	1.3	3
SI-547b	1.37	191	123	—	38.88	0.64	51.0	1.8			
SI-548a	19.57	50	30	—	13.19	0.85	50.6	1.9			

Note: FT—correction factor for alpha-ejection loss; nd—not determined (possibly micro-inclusions); MSWD—mean square of weighted deviates.



Figure 7. Field photo of south-dipping, unnamed calcareous arenite sequence along the Pacora River (located in Fig. 1). This unit contains large foraminifera identified as Oligocene (SI-3775 and SI-2662), and is found resting unconformably along the southern flank of the San Blas Range on deformed basement rocks, both plutonic and volcanic.

feldspar percentage is low throughout the unit (Fig. 8A). A lithic sandstone in the upper part of the Culebra Formation yielded 102 zircon grains that we dated using U/Pb geochronology (Fig. 8C). This sample contains significant populations at 52 Ma ($n = 94$), 30 Ma ($n = 3$), and 19 Ma ($n = 5$), thus the upper Culebra Formation can only be 19 Ma or younger.

The lowermost facies of the Culebra Formation is variable and contains lignitic mudstone, medium-grained calcarenite, black mudstone, and shale, or coaly shale. This variable sequence overlies strata of the Las Cascadas Formation. The calcareous Emperador Member (*sensu* Kirby et al., 2008) contains 22 species from 14 genera of coral reef with a succession that

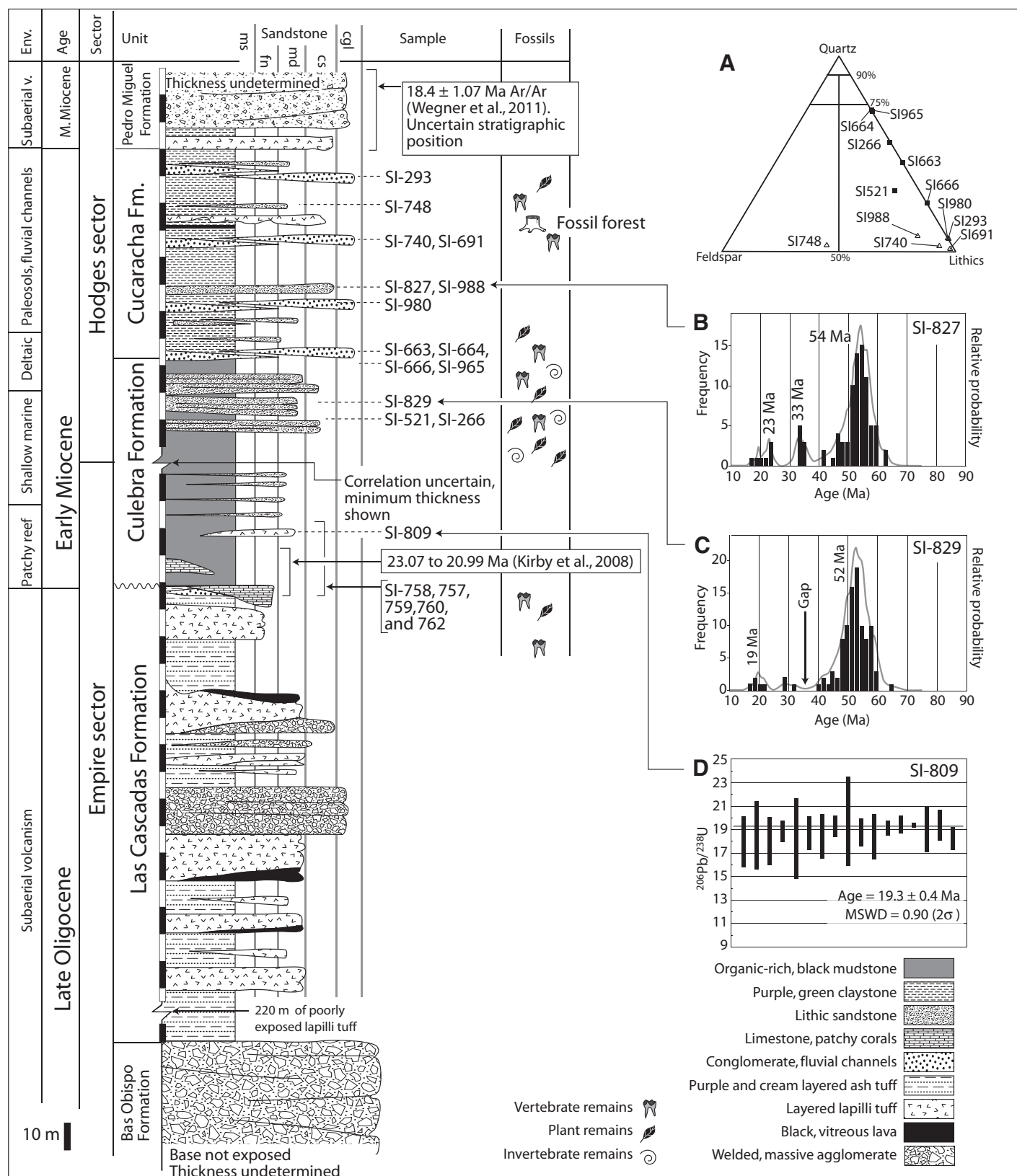


Figure 8. Stratigraphic column measured in surface exposures along the Panama Canal. (A) QFL (quartz, feldspar, lithics) composition diagram for Cucaracha and Culebra arenites; (B–C) U/Pb ages in detrital zircons recovered from Cucaracha and Culebra Formations, respectively; and (D) U/Pb ages in magmatic zircons recovered from a felsic tuff near the base of the Culebra Formation. MSWD—mean square of weighted deviates. See Table 1 for sample coordinates and GSA Data Repository for sample descriptions and coordinates (see text footnote 1).

includes 20 m of reef carbonates (Johnson and Kirby, 2006). Sr isotopic dating (Kirby et al., 2008) from seven carbonates samples (corals, ostreids, and pectinids) yielded age estimates for the Culebra from 23.07 Ma (lower Culebra Formation) to 20.99 Ma and 21.24 Ma (Emperador Member) to 19.12 Ma and 19.38 Ma (upper Culebra Formation). The age of the uppermost Culebra Formation is between 18.8 Ma and 14 Ma based on land mammal biostratigraphy (Kirby et al., 2008), in good agreement with detrital geochronology (Fig. 8C).

Calcareous nannofossils extracted from the base of the Culebra Formation (Table 1; Fig. 8) indicate an early Miocene age (Burdigalian to Aquitanian, 23.03–15.97 Ma) and consist of *Helicosphaera euphratis*, poorly preserved *Sphenolithus* specimens thought to be *Sphenolithus disbelemnus* or *Sphenolithus conicus*. Other forms indicate middle to early Miocene ages, with common *Cyclicargolithus floridanus* and *Coccolithus miopelagicus*. The age of the base of the Culebra Formation is additionally constrained by 17 zircons recovered from a 1-m-thick, felsic, welded lapilli crystalline tuff near the base of the unit (Fig. 8D), yielding a weight average age of 19.3 ± 0.4 Ma. Although the pyroclastic nature of this bed could potentially mix juvenile and older magmatic material, the concordant nature of the analyzed zircon population suggests that this age represents the magmatic crystallization of the volcanic rock. In the absence of additional criteria, it can be safely stated that this tuff is 19.3 Ma or younger.

The Cucaracha Formation (Fig. 8) is a heterogeneous continental siliciclastic unit (Retallack and Kirby, 2007) characterized by red, green, and purple mudstone interbedded with lithic arenites, pebble conglomerate beds, and a tuff layer toward the top. The upper contact of the Cucaracha Formation in Hodges Hill is a sharp and slightly angular unconformity, above which the relief-forming lavas and tuffs of the Pedro Miguel Formation lie. The sandy fraction of the Cucaracha Formation is lithic and feldspathic (Fig. 8A; SI-293, SI-748, SI-740, SI-988, SI-980). In average, sandstones show low quartz (<10%) and feldspar content (<15%), whereas the lithic percentage is high (>75%). The lithic fragments are highly weathered and are represented mostly by tuffs with lesser amounts of basalt and plutonic fragments.

Land mammal biostratigraphy based on the rich fauna found in this unit suggests an age between 18 and 17 Ma (Kirby et al., 2008). Ninety detrital zircons grains were recovered from a lithic sandstone from the lower part of the Cucaracha Formation (Fig. 8B). It contained

representative populations at ca. 20 Ma ($n = 3$), 23 Ma ($n = 4$), 33 Ma ($n = 8$), 42 Ma ($n = 8$), and 54 Ma ($n = 49$). No magmatic zircons could be recovered from samples of the felsic tuff near the top of the Cucaracha Formation (Fig. 8); however, two potassium-argon ages on this tuff were reported by Woodring (1982) at 22.2 ± 1.7 and 18.9 ± 2.2 Ma. An 18.4 ± 1.0 Ma Ar/Ar age was reported in excavation sites of the Canal Basin, near current exposures of the Pedro Miguel Formation (Wegner et al., 2011); the exact stratigraphic position of this sample, however, could not be determined (Fig. 8).

DISCUSSION

In the following discussion, we integrate field mapping and stratigraphic observations in the sedimentary basins of central Panama with our new geochronological and cooling data to show the correlation among granitoid intrusion, exhumation, and deformation, and the sedimentary record of these events (Fig. 9).

Age of Basement Complex and Its Early History

Our geochronological data confirm work in the San Blas Range and the Canal Basin by earlier workers (Lissina, 2005; Wegner et al., 2011) that documented a Late Cretaceous initiation of magmatic activity continuing into Eocene times. Our new data allow us to further refine this characterization to show that the magmatic activity that continued uninterrupted west of the Canal Basin (e.g., Speidel et al., 2001) was absent from 38 to 28 Ma in the Canal Basin and east of it, and restarted after 28 Ma in a different geographic position (Lissina, 2005).

Most of our U/Pb determinations in central Panama (Fig. 1, inset; Fig. 4), as well as our detrital zircon samples (Figs. 8B and 8C), show peak populations in the 39–58 Ma age range. As mentioned already, we recognize a paucity in the radiometric age determinations in the 38–28 Ma interval from in situ records east of the Canal Basin (Fig. 1, inset), and detrital zircon records preserved in the lower Miocene strata of the Canal Basin (Figs. 8B and 8C).

Our data support Lissina's (2005) suggestion of a geographic shift in the axis of volcanic activity, with magmatic products older than 38 Ma offset between Azuero and San Blas (Fig. 1), whereas younger magmatic products define a continuous, uninterrupted magmatic axis (Fig. 1). In the Canal Basin, the Bas Obispo Formation is the first record of renewed magmatism at 25.3 ± 0.13 Ma (Rooney et al., 2010), with intense activity preserved as the volcaniclastic Las Cascadas Formation (Fig. 9), minor

volcanism recorded in the Culebra Formation (a tuff at 19 ± 0.4 Ma; Fig. 8D), and more widespread younger volcanics in the Cucaracha (starting with the ash tuff in Fig. 8) and Pedro Miguel Formations (Woodring, 1957). No magmatism is present east of the Canal after ca. 15 Ma (Fig. 1, inset).

Exhumation and Deformation of the Basement Complex

Significant cooling of the 58–54 Ma Cerro Azul granitoids (Fig. 4) started in Lutetian time (47–42 Ma), as documented by fission-track data in apatite and (U-Th)/He data in zircon (Fig. 5), implying an ~10 m.y. gap between emplacement and initiation of cooling. Two distinct phases of regional cooling are expressed by well-defined age-elevation relationships with steep positive correlations and virtually concordant ages at 2 σ : (1) 47–42 Ma as indicated by AFT and (U-Th)/He analyses in zircon; and (2) 12–9 Ma as recorded by helium analyses in apatite (Fig. 5). The earlier cooling event must have brought the Cerro Azul granitoids from temperatures beyond those where helium is partially retained in zircon (~200 °C; Farley, 2000; Reiners, 2005) to temperatures where apatite fission tracks are stable (~70 °C; Green et al., 1985; Gleadow et al., 1986) in the 47–42 Ma interval.

Even though the Eocene cooling episode (47–42 Ma) could be interpreted to result from postmagmatic cooling, our preferred interpretation is exhumation. There are two reasons to favor exhumation: (1) the concordant nature of (U-Th)/He analyses in zircon and AFT ages over crustal depths spanning ~900 m; and (2) a marked, regional angular unconformity (Figs. 2 and 3) where terrestrial to shallow-marine strata of late Eocene to Oligocene age (Gatuncillo Formation and unnamed limestone of Fig. 2) directly rest on deformed basement rocks. This unconformity documents an early to middle Eocene period of deformation and erosion that removed the entire thickness of the volcaniclastic basement complex (Fig. 3) in the center of the geologic map (Utiye-Mamoni, Fig. 2), so that upper Eocene to Oligocene strata (SI-3775, SI-2662, Fig. 2) directly rest on plutonic rocks of Paleocene age (e.g., SI-540, SI-542, SI-543 in Figs. 2 and 4). This period of erosion coincides with Lutetian cooling recorded by low-temperature thermochronology in Cerro Azul (47–42 Ma), and the left-lateral offset of the older magmatic arc (starting at ca. 40 Ma; Lissina, 2005), while predating the magmatic gap described previously herein (38–28 Ma). Assuming a minimum 80–90 °C cooling and a paleogeothermal gradient of 20–30 °C/km,

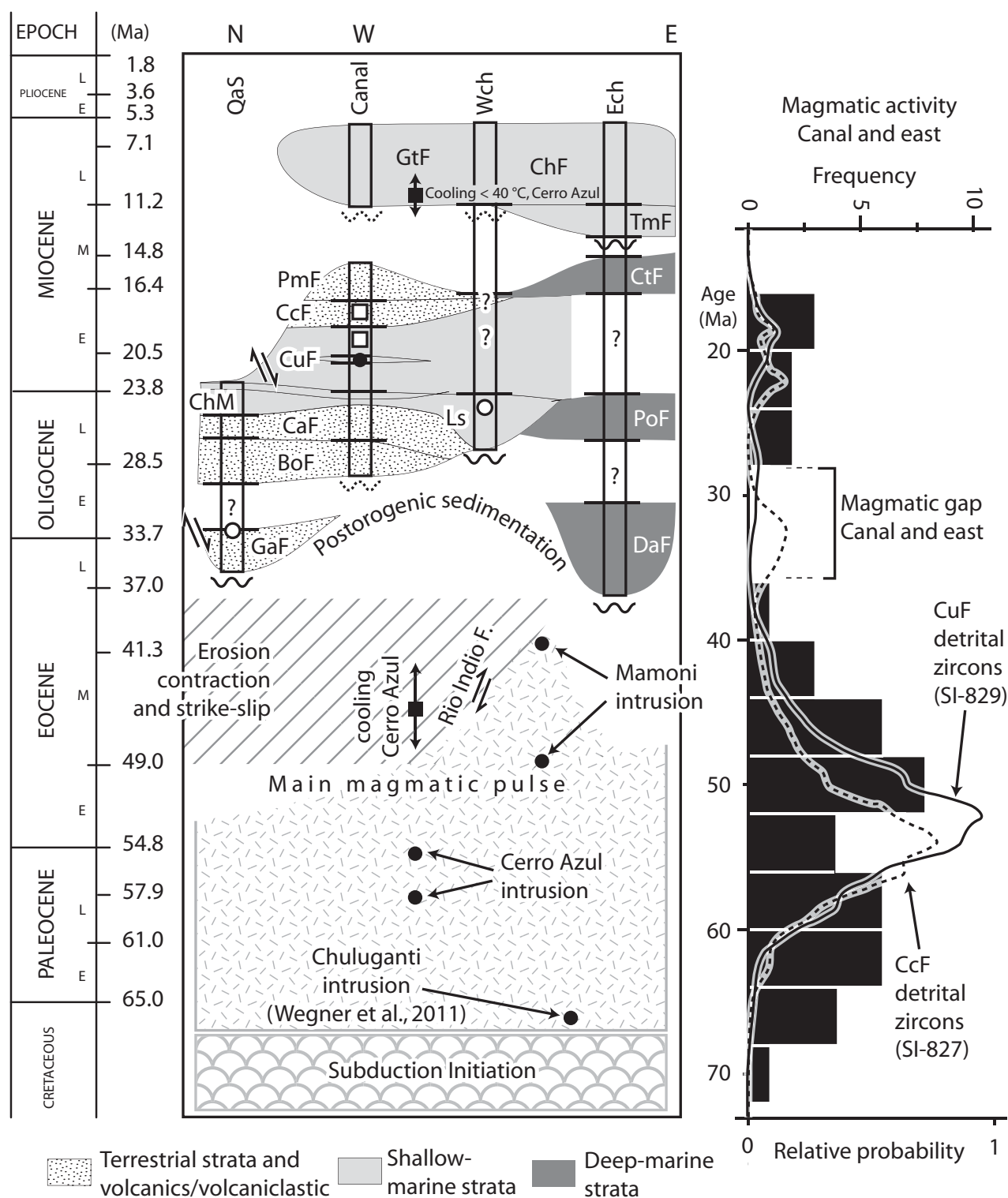


Figure 9. Synoptic diagram showing events and strata in the Canal Basin and east of it. Canal Basin and Quebrancha syncline (Qas) are after Woodring (1957); eastern Chucunaque (Ech) strata are after Coates et al. (2004). BoF—Bas Obispo and Bohio Formations; CaF—Las Cascadas and Caimito Formations; CcF—Cucaracha Formation; ChM—Chilibrillo Member; CtF—Clarita Formation; CuF—Culebra Formation; DaF—Darien Formation; GaF—Gatuncillo Formation; GtF—Gatun Formation; Ls—unnamed limestone; PmF—Pedro Miguel Formation; PoF—Pocorna Formation; TmF—Tapaliza and Membrillo Formations; Wch—western Chucunaque. Black dots represent geochronologic control points, white dots represent paleontological determinations, black squares are thermochronological data, and white squares are detrital geochronological data discussed in text. Right side: comparison between in situ age determinations (from histogram in Fig. 1 and detrital records of Figs. 8B and Fig. 8C).

~3–5 km of crustal section were removed from the middle Eocene to the present, which is roughly similar to the estimated thickness of the volcanoclastic basement (Fig. 3). The basement complex and sedimentary cover were not significantly buried afterward, as no Miocene strata are found resting unconformably on either basement or older cover strata (Fig. 2).

The second phase of exhumation cooling below 40 °C between 12 and 9 Ma, recorded by (U-Th)/He analyses in apatite (Fig. 5) in the Cerro Azul massif, is consistent with results of detailed paleobathymetric analyses in the easternmost Chucunaque and Canal Basins (Coates *et al.*, 1992, 2004; Collins *et al.*, 1995, 1996). The paleobathymetric analyses indicate shallowing to inner neritic conditions at this time, and they are interpreted to record the initiation of collision with South America along the Uramita fault (Fig. 1). The geologic map (Fig. 2, inset) shows north-trending strike-slip faults that intersect and displace both basement complex and cover sequence. These faults and the mild folding affecting the cover sequences of central Panama may be an indication of this younger deformation activity.

Additional Constraints on Exhumation

Detrital zircon geochronology serves as independent criteria to test times of exhumation and unroofing of the arc. Zircon populations preserved in sandstone contain the record of exposed, eroding, felsic plutonic massifs at the time of accumulation of the strata. Lithic sandstone samples of the Gatuncillo Formation in the Quebrancha syncline yielded no detrital zircons (Table 1), as only the zircon-poor, basaltic volcanoclastic basement was being unroofed in this part of the isthmus (Quebrancha syncline, Fig. 2). The first detrital record of the erosion of the basement complex granitoids is found in immature, first-cycle lithic arenite of the lower Miocene Culebra and Cucaracha Formations in the Canal Basin (Fig. 8). Samples SI-827 and SI-829 (Figs. 8B and 8C) mimic the signal extracted from the *in situ* plutonic basement ages in the Isthmus of Panama (Fig. 9, right side). These signatures result from erosion of granitoids rich in zircon and indicate that the plutonic arc root was exposed during early Miocene time. The detrital zircon population recovered from the Culebra Formation suggests a provenance from the northeast, as the signal follows the *in situ* record east of the Canal Basin closely (Fig. 9). A mixed provenance may be suggested for the Cucaracha Formation, where a 33 Ma population (Fig. 8B), absent from the *in situ* record east of the Canal Basin, is present west of the Canal Basin (Fig. 1, inset).

Paleogeographic Implications

The homogeneity of the San Blas Range–Chucunaque Basin (Fig. 1) pair suggests that the results presented here for central Panama could be broadly valid for the entire San Blas Range. Regional geologic maps show that the axis of this basin-range pair is continuous and homogeneous and shows no trace of intervening tectonic boundaries, crosscutting sutures, grabens (Mann and Corrigan, 1990; Coates *et al.*, 2004), or geophysical anomalies (Westbrook, 1990). The axis of this range-basin pair is maintained as far east as the Atrato Basin (Duque-Caro, 1990) and Mande-Acandi batholiths (Aspden *et al.*, 1987). The late Miocene (12–9 Ma) cooling below 40 °C recorded in the Cerro Azul granitoids (Fig. 5) is also documented in the easternmost Chucunaque Basin as a shallowing event (Coates *et al.*, 2004, and references therein), so this basin-range pair seems to have behaved as a single tectonic unit (Fig. 1).

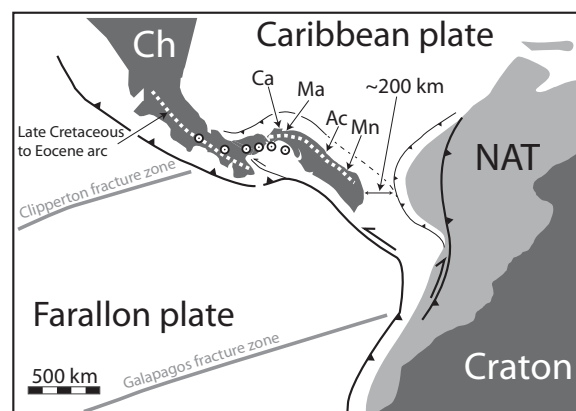
This study shows that the central part of the Isthmus of Panama, and also probably the entire San Blas Range, was being eroded starting in late Eocene times through Oligocene and Miocene times. Thus, the paleogeographic configuration from the moment of amalgamation with North America through the Chortis block (early Miocene; Kirby and MacFadden, 2005) is that of a peninsula that straddled the Canal Basin and included most of the San Blas Range (Fig. 10). When placed in a paleogeographic space (Fig. 10), it greatly reduces the width and depth of the strait that once separated southern Central America from South America, leaving a very narrow isthmian strait that may have favored the start of early faunal exchanges of frogs, fish, and plants in the middle to late Miocene (e.g.,

Birmingham and Martin, 1998; Weigt *et al.*, 2005; Cody *et al.*, 2010). A late Oligocene to early Miocene initiation of collision between the easternmost tip of the Central American arc and northwestern South America (Farris *et al.*, 2011) would imply that the continuous isolation of land mammals until the late Pliocene Great American Interchange (Marshall *et al.*, 1982) was the result of a wet and hot climate in the isthmus. This may have stalled mammal interchange until ice sheets formed on Canada and savanna-like environments developed in Panama (Molnar, 2008).

CONCLUSIONS

The integration of field mapping, U/Pb geochronology of magmatic zircons, provenance analyses, and thermochronology allows definition of a sequence of events in the central part of the Isthmus of Panama: (1) subduction-related, latest Cretaceous (Wegner *et al.*, 2011) to middle Eocene arc magmatism with ages between 58 and 39 Ma; (2) initial exhumation cooling of parts of the basement complex from more than ~200 °C to less than 60 °C in the interval 47–42 Ma; (3) pre-late Eocene north-verging deformation of the volcanic and plutonic basement complex, temporary cessation of magmatic activity east of the Canal Basin in late Eocene to late Oligocene time (38–28 Ma), and accumulation of the partially terrestrial upper Eocene to Oligocene strata; (4) reinitiation of arc magmatism at ca. 25 Ma and accumulation of terrestrial and shallow-marine strata and volcanic products in the Canal and western Chucunaque Basins; (5) continual emergence and erosion of the roots of the arc by early Miocene time as recorded by detrital zircon signatures in the Canal

Figure 10. Late Oligocene–early Miocene reconstruction showing a segmented Late Cretaceous to Eocene magmatic arc (thick, dashed, white line), and a ca. 25 Ma and younger arc (represented by dots). The San Blas Range is treated as a single tectonic unit that has emerged since late Eocene times, is continuous into the Baudo Range of western Colombia, and has a land connection to North America (Kirby and MacFadden, 2005). Configuration of north Andean terranes (NAT) is after Montes *et al.* (2010), Farallon plate is after Lonsdale (2005), Chortis (Ch) and the craton relative positions are after tectonic reconstructions (Pindell and Kennan, 2009; Farris *et al.*, 2011) using GPlates (Boyden *et al.*, 2011). Paleogene granitoids: Ac—Acandi, Ca—Cerro Azul, Ma—Mamoni, Mn—Mande Batholith (Aspden *et al.*, 1987; this study).



Basin; and (6) late Miocene exhumation cooling below 40 °C in the Cerro Azul area, and shallowing marine sedimentation in the easternmost Chucunaque Basin (Coates et al., 2004). These findings are interpreted to show that the San Blas Range, as a single tectonic unit east of the Canal Basin (Fig. 1), was emergent above sea level starting in late Eocene time through Oligocene and Miocene time, becoming a peninsula of North America since early Miocene time (Whitmore and Stewart, 1965; Kirby and MacFadden, 2005). This paleogeographic configuration greatly restricts the width of the seaway separating the Pacific and Caribbean waters since early Miocene times.

APPENDIX: DETAILED METHODS

U/Pb Geochronology

The U/Pb geochronology was conducted using an isoprobe equipped with an ArF excimer laser ablation system, which has an emission wavelength of 193 nm. The collector configuration allows measurement of ^{204}Pb in the ion-counting channel while ^{206}Pb , ^{207}Pb , ^{208}Pb , ^{232}Th , and ^{238}U are simultaneously measured with Faraday detectors. All analyses were conducted in static mode with a laser beam diameter of 35 μm , operated with output energy of ~32 mJ (at 23 kV) and a pulse rate of 8 Hz. Each analysis consisted of one 12 s integration on peaks with no laser firing and twenty 1 s integrations on peaks with the laser firing. The ablated material was carried with helium gas into the plasma source. Hg contribution to the ^{204}Pb mass position was removed by subtracting on-peak background values. Inter-element fractionation was monitored by analyzing fragments of a large Sri Lanka zircon standard, which has a concordant thermal ionization mass spectrometry (TIMS) age of 564 ± 3.2 Ma (2σ) (Gehrels et al., 2008). The lead isotopic ratios were corrected for common Pb using the measured ^{204}Pb , assuming an initial Pb composition according to Stacey and Kramers (1975) and respective uncertainties of 1.0, 0.3, and 2.0 for $^{206}\text{Pb}/^{204}\text{Pb}$, $^{207}\text{Pb}/^{204}\text{Pb}$, and $^{208}\text{Pb}/^{204}\text{Pb}$.

Apatite Fission Track

Apatite crystals were obtained from plutonic rock samples using conventional gravimetric (Gemini® water table and TBE-MeI heavy liquids) and magnetic (Frantz Isodynamic®) separation techniques. Apatite crystals were mounted in epoxy squares (1.5 cm²) and cured at ~60 °C. Subsequently, grain internal surfaces were exposed by grinding and polishing to an optical finish. To reveal spontaneous fission tracks, mounts were etched using 5.5 M HNO₃ for 20.0 ± 0.5 s at $\sim 21.0 \pm 0.5$ °C. Mounts were scanned under a petrographic microscope at high magnification (400 \times) to select the best-suited apatite grains for age determinations. Selected grains were recorded in a mount-specific coordinate system for easy location both in the petrographic microscope for track counting and in the LA-ICP-MS system for U/Ca spectrometric measurements. Fission tracks were counted on approximately 35 grains or more per sample (except for samples 060042, 9 grains; SD008, 13 grains; and SD006, 22 grains). Grain locations where track counting took place were carefully recorded in the proper coordinate

system for each mount for subsequent spectrometric analysis over the same region on each apatite crystal dated. At each spot, 30 scans for ^{238}U , ^{232}Th , ^{147}Sm , and ^{43}Ca were performed. The first 10 scans were used for background measurements by measuring with a shut laser beam. Fission-track ages and errors were calculated from the ratio track density/ ^{238}U using a modified version of the radioactive decay equation that includes ζ_{MS} , a LA-ICP-MS zeta calibration factor (Donelick et al., 2005). Zeta calibration factors were used to derive ages for all of the samples dated. Zeta is generated at the beginning and end of each LA-ICP-MS session by measuring the $^{238}\text{U}/^{43}\text{Ca}$ ratio in the Durango (31.44 ± 0.09 Ma) apatite standard. Throughout the analytical procedure, AFT ages for Durango standard were virtually identical to reported ages (31.4 ± 1.6 Ma). Horizontal confined track lengths were measured in all 10 samples. To enhance measurability of populations of confined natural tracks, apatite aliquots of each mount were irradiated by a ^{252}Cf source in a vacuum for 140 min (Donelick and Miller, 1991). Irradiated samples were etched under the same conditions described previously. Only natural, fully etched, horizontal, and confined tracks were measured for both length (± 0.2 μm) and angle to the c axis ($\pm 2^\circ$). Track lengths reported are corrected for c -axis orientation, which yields slightly higher figures. Apatite fission-track analyses were performed at 2000 \times magnification under nonpolarized light. Appropriate track lengths were measured using a projection tube and a digitizing tablet, calibrated using a stage micrometer. We conducted track calculations against apatite standards of the Cerro de Mercado, Durango (Mexico), and Fish Canyon Tuff (USA). Because kinetics of apatite fission-track annealing are a function of chemical composition (Green et al., 1985; O'Sullivan and Parrish, 1995; Carlson et al., 1999) and mineralogical properties (Donelick et al., 1999; Barbarand et al., 2003) of the analyzed apatite crystals, we took potential kinetic variability in our samples into consideration by using Dpar as a parameter. Dpar is routinely used as a proxy for the annealing kinetics of apatite grains (Burtner et al., 1994; Barbarand et al., 2003; Donelick et al., 2005; Restrepo-Moreno et al., 2009), and it is defined as the diameter of the fission-track etch pit parallel to the crystallographic c axis of the apatite crystal at the polished and etched surface of the analyzed grain (Ketcham et al., 1999; Donelick et al., 2005). Age and track-length measured apatite grains were classified for annealing kinetics with Dpar. For each grain measured for age or track length, we recorded between 1 and 5 Dpar values and determined a mean Dpar. Apatite fission-track ages, track lengths, and Dpar data combine to provide information that can be used to constrain a sample's thermal history with inverse modeling. Apatite fission-track data for representative samples, i.e., fission-track ages, track lengths, and Dpar measurements, were used for developing time-temperature paths through inverse Monte Carlo modeling used in the HeFTy® software (Ketcham, 2008). Specifically, the 1.6.7 version of HeFTy® is based on the multikinetic annealing model of Ketcham et al. (2007), with c -axis projected track-length data (Ketcham et al., 2007). For modeling purposes, each sample was constrained to a subsurface temperature between 140 °C and 160 °C at a time somewhat older than the AFT age, and present-day surface temperature at the elevations where samples were collected typically around 20–25 °C. The modeling approach was to use a single, broad sampling space so as to allow models as much freedom as possible. As we expect these samples from an active orogen to reflect relatively simple cooling histories, cooling

paths were defined as monotonic and composed of 16 random segments to allow for sufficient variability in the exhumation path. The Dpar kinetic parameter was used to calibrate annealing parameters as well as initial confined track lengths. All the thermal histories were calculated using fission-track lengths projected onto the crystallographic c axis using the method of Donelick et al. (1999). Goodness of fit between modeled and measured track length distributions was assessed using the Kolmogorov-Smirnov test, with merit values of 0.5 and 0.05 for good and acceptable fits, respectively.

Helium Dating in Zircon

Measurements of parent and daughter nuclides in zircon grains were performed on two single-grain aliquots per sample following the protocol presented in Reiners (2005). Selected crystals were photographed and their dimensions measured in two perpendicular perspectives parallel to the a_1 and a_2 crystallographic axes. Measured dimensions and an assigned morphology were used to calculate the alpha ejection correction following the Ft correction scheme of Farley (2002). The extraction involved placement of a single crystal into an ~1 mm Nb foil packet that was then slightly closed and placed on a Cu planchet with another few dozen sample slots in a high-vacuum sample chamber connected to the He purification/measurement line. Each foil packet was directly heated using a 10 μm focused laser beam of a 1064 nm Nd-YAG laser to ~1100–1250 °C for 15 min extraction intervals. All samples were then subjected to at least two degassings of the crystal (typical re-extracts yielded less than 0.5% of previous ^4He values). Helium extracted from zircons was spiked with ~0.1–1.0 pmol ^3He , cryogenically concentrated and purified, and expanded into a small volume with a gas-source quadrupole mass spectrometer. Ratios of $^4\text{He}/^3\text{He}$ were measured for about 10 s following gas release and nominal equilibration time. Measured ratios were corrected for background and interferences on mass 3 (HD+ and H3+), and compared with $^4\text{He}/^3\text{He}$ measured on pipetted aliquots of a manometrically calibrated ^4He standard processed by the same methods. The ^4He in the unknown zircon is assumed to be the product of the ^4He content of the standard, with $^4\text{He}/^3\text{He}$ ratio measurements on the unknown and the standard. Uranium and thorium nuclides in degassed zircons were measured by isotope dilution and solution ICP-MS. The approach required spiking the sample with an isotopically distinctive U-Th spike, sample-spike equilibration, and dissolution to a final solution suitable for ICP-MS. Zircon dissolution was carried out using HF-HNO₃ mixtures, which can dissolve the entire Nb foil and zircon content in Parr bombs at temperatures and pressures higher than ambient. Ratios of $^{238}\text{U}/^{235}\text{U}$ and $^{232}\text{Th}/^{230}\text{Th}$ were quantified by 2000 measurements of the average intensities in the middle 10% of peak widths in low-resolution mode on an Element2 high-resolution ICP-MS. The $^{238}\text{U}/^{235}\text{U}$ ratio was also measured to check for Pt contamination and mass fractionation. The zircon content in U and Th was calculated from multiple determinations of isotope ratios on pure spike and spiked normals containing 1–4 ng of isotopically normal U and Th. In zircon, He dating alpha ejection was corrected using the method of Farley (2002). The analyzed standard included zircons from the Fish Canyon Tuff with two standard analyses per sample batch. This standard has been routinely calibrated, yielding a (U-Th)/He age of 28.29 ± 0.26 Ma in 114 grains

(95%; 2σ external error of 2.6 Ma or 9.3%, mean square of weighted deviates [MSWD] = 20). Fish Canyon zircon analyses carried out during this work are included with the results.

Propagated errors for zircon He ages based on the analytical uncertainty associated with U, Th, and He measurements are ~4% (2σ) for laser samples (Farley, 2002; Reiners, 2005). Nevertheless, a 6% (2σ) uncertainty for all samples is reported based on the reproducibility of replicate analyses of laboratory standard samples (Reiners, 2005).

Apatite Helium Dating

Single-grain aliquots were prepared, and two replicate analyses were performed for each sample. After careful optical screening, apatite crystals were placed into 0.8 mm Nb packets, which were then loaded into stainless-steel sample planchets. Each sample replicate was degassed via laser heating for 3 min utilizing a Nd-YAG laser at 1.5 W to attain temperatures of ~1050 °C and then analyzed for ^4He , followed by a second extraction (He re-extraction) to ensure complete degassing and to monitor He release from more retentive U- and Th-bearing inclusions in analyzed apatite. Helium blanks (0.05–0.1 fmol ^4He) were determined by heating empty Nb foil packets using the same procedure. Gas extracted from samples was processed by: (1) spiking with ~4 pmol of ^3He ; (2) concentrating in a cryogenic system at 16 K on a charcoal trap, and purification by release at 37 K; and (3) measuring $^4\text{He}/^3\text{He}$ ratios (corrected for HD and H₃ by monitoring H⁺) on a quadrupole mass spectrometer. All ratios were referenced to multiple same-day measured ratios and known volumes of ^4He standards processed in a similar fashion.

Once ^4He measurements were completed, samples were retrieved from the laser cell, placed in Teflon vials, dissolved in ~30% HNO_3 , and spiked with mixed ^{230}Th – ^{235}U – ^{149}Sm tracer for isotope dilution ICP-MS analysis of U, Th, and Sm. Each batch of samples was prepared with a series of acid blanks and spiked normals to monitor the purity and calibration of reagents and spikes. Spiked samples were analyzed as 0.5 mL of ~1.5 ppb U–Th solutions by isotope dilution on a Thermo Element 2 ICP-MS. Precision and sensitivity of the instrument allow isotopic analyses with RSD (relative standard deviation) <1%. Concentrations of ^{147}Sm were close to zero for all samples. Th/U ratios were used to monitor for the presence of Th-rich phases such as monazite. The mean Th/U for all of the replicates combined was 0.9, and most values were below 1, so none of the analyses had to be excluded. Alpha ejection was corrected for apatite He ages using the method of Farley et al. (2002). Durango apatite standards were run during each batch of unknown samples (every 9 unknowns) to monitor system performance and check analytical accuracy. Replicate aliquots of this standard yield an average age of 31.9 Ma, with two standard deviations of 2.2 Ma (6.6%), and a weighted mean age and error of 31.94 ± 0.17 Ma (95% confidence interval, with a 2σ required external error of 1.9 Ma or 5.9%, MSWD = 5.4). Analytical uncertainties for the University of Arizona (U–Th)/He facility are assessed at ~6% (2fD), which incorporate noble gas analysis and ICP-MS uncertainties. Propagated errors for apatite He ages based on the analytical uncertainty associated with U, Th, and He measurements are 4% (2σ) for laser samples. A 6% (2σ) uncertainty for all samples is reported based on the reproducibility of replicate analysis of laboratory standard samples (Reiners, 2005).

ACKNOWLEDGMENTS

This project was supported by ACP (Panama Canal Authority) contract SAA-199520-KRP; Senacyst grants SUM-07-001 and EST010-080 A; Colciencias, U.S. National Science Foundation (NSF) grant 0966884 (OISE, EAR, DRL), Mark Tupper, NSF EAR-0824299, National Geographic, Smithsonian Institution, and Ricardo Perez S.A. Thanks go to H. Broce, F. Guardia, P. Francesci, V. Luque, A. Baresh, F. Moreno, and L. Oviedo for their help. G. Wörner kindly provided early copies of his manuscripts and data. Access to field areas and collection permits were granted by ACP, Ministerio de Industria y Comercio, and Odebrecht. We are grateful to P. Molnar, S. Johnston, J. Pindell, P. Mann, D. Foster, and P. O'Sullivan, as well as to all participants of the February 2010 IGCP (International Union of Geological Sciences) 546 "Subduction Zones of the Caribbean" and IGCP 574 "Bending and Bent Orogens, and Continental Ribbons" for their critical reviews.

REFERENCES CITED

- Aspden, J.A., McCourt, W.J., and Brook, M., 1987, Geometrical control of subduction-related magmatism: The Mesozoic and Cenozoic plutonic history of western Colombia: *Journal of the Geological Society of London*, v. 144, p. 893–905, doi:10.1144/gsjgs.144.6.0893.
- Barbarand, J., Carter, A., Wood, L., and Hurford, A.J., 2003, Compositional and structural control of fission-track annealing in apatite: *Chemical Geology*, v. 198, p. 107–137, doi:10.1016/S0009-2541(02)00424-2.
- Birmingham, E., and Martin, A.P., 1998, Comparative mtDNA phylogeography of Neotropical freshwater fishes: Testing shared history to infer the evolutionary landscape of lower Central America: *Molecular Ecology*, v. 7, p. 499–517, doi:10.1046/j.1365-294x.1998.00358.x.
- Beu, A.G., 2001, Gradual Miocene to Pleistocene uplift of the Central American isthmus: Evidence from Tropical American Tonoidean gastropods: *Journal of Paleontology*, v. 75, no. 3, p. 706–720, doi:10.1666/0022-3366(2001)075<0706:GMTPUO>2.0.CO;2.
- Blacut, G., and Klempell, R.M., 1969, A stratigraphic sequence of benthonic smaller foraminifera from the La Boca Formation, Panama Canal Zone: Contributions from the Cushman Foundation for Foraminiferal Research, v. 20, no. 1, p. 1–22.
- Boyden, J., Müller, R.D., Gurnis, M.S., Torsvik, T., Clark, J.A., Turner, M., Ivey-Law, H., Watson, R.J., and Cannon, J.S., 2011, Next-generation plate-tectonic reconstructions using GPlates, in Keller, G.R., and Bar, C., eds., *Geoinformatics: Cyberinfrastructure for the Solid Earth Sciences*: Cambridge, UK, Cambridge University Press, p. 95–113.
- Buchs, D.M., Arculus, R.J., Baumgartner, P.O., Baumgartner-Mora, C., and Ulianov, A., 2010, Late Cretaceous arc development on the SW margin of the Caribbean plate: Insights from the Golfo (Costa Rica) and Azuero (Panama) complexes: *Geochemistry, Geophysics, Geosystems*, v. 11, no. 7, Q07S24, doi:10.1029/2009GC002901.
- Burner, R.L., Nigrini, A., and Donelick, R.A., 1994, Thermochronology of lower Cretaceous source rocks in the Idaho-Wyoming thrust belt: The American Association of Petroleum Geologists Bulletin, v. 78, p. 1613–1636.
- Burton, K.W., Ling, H.-F., and O'Nions, R.K., 1997, Closure of the Central American isthmus and its effect on deep-water formation in the North Atlantic: *Nature*, v. 386, no. 6623, p. 382–385, doi:10.1038/386382a0.
- Carlson, W.D., Donelick, R.A., and Ketcham, R.A., 1999, Variability of apatite fission-track annealing kinetics: I. Experimental results: *The American Mineralogist*, v. 84, p. 1213–1223.
- Coates, A.G., Jackson, J.B.C., Collins, L.S., Cronin, T.M., Dowsett, H.J., Bybell, L.M., Jung, P., and Obando, J.A., 1992, Closure of the Isthmus of Panama; the near-shore marine record of Costa Rica and western Panama: *Geological Society of America Bulletin*, v. 104, no. 7, p. 814–828, doi:10.1130/0016-7606(1992)104<0814:COTIOP>2.3.CO;2.
- Coates, A.G., Collins, L.S., Aubry, M.-P., and Berggren, W.A., 2004, The geology of the Darien, Panama, and the late Miocene–Pliocene collision of the Panama arc with northwestern South America: *Geological Society of America Bulletin*, v. 116, no. 11–12, p. 1327–1344, doi:10.1130/B25275.1.
- Cody, S., Richardson, J.E., Rull, V., Ellis, C., and Pennington, T., 2010, The Great American Biotic Interchange revisited: *Ecography*, v. 33, p. 326–332.
- Cole, W.S., 1949, Upper Eocene larger foraminifera from the Panama Canal Zone: *Journal of Paleontology*, v. 23, no. 3, p. 267–275.
- Cole, W.S., 1953, Some late Oligocene larger foraminifera from Panama: *Journal of Paleontology*, v. 27, no. 3, p. 332–337.
- Collins, L.S., Coates, A.G., Jackson, J.B.C., and Obando, J.A., 1995, Timing and rates of emergence of the Limon and Bocas del Toro basins: Caribbean effects of Cocos Ridge subduction?: *Geological Society of America Bulletin*, v. 295, p. 263–289.
- Collins, L.S., Coates, A.G., Berggren, W.A., Aubry, M.-P., and Zhang, J., 1996, The late Miocene Panama isthmian strait: *Geology*, v. 24, no. 8, p. 687–690, doi:10.1130/0091-7613(1996)024<0687:TLMPIS>2.3.CO;2.
- Corfu, F., Hanchar, J.M., Hoskin, P.W.O., and Kinny, P., 2003, Atlas of zircon textures: Reviews in Mineralogy and Geochemistry, v. 53, p. 469–500, doi:10.2113/0530469.
- de Boer, J.Z., Defant, M.J., Stewart, R.H., and Bellon, H., 1991, Evidence for active subduction below western Panama: *Geology*, v. 19, no. 6, p. 649–652, doi:10.1130/0091-7613(1991)019<0649:EFASBW>2.3.CO;2.
- Defant, M.J., Clark, L.F., Stewart, R.H., Drummond, M.S., De Boer, J.Z., Maury, R.C., Bellon, H., Jackson, T.E., and Restrepo, J.F., 1991a, Andesite and dacite genesis via contrasting processes: The geology and geochemistry of El Valle Volcano, Panama: Contributions to Mineralogy and Petrology, v. 106, no. 3, p. 309–324, doi:10.1007/BF00324560.
- Defant, M.J., Richerson, P.M., De Boer, J.Z., Stewart, R.H., Maury, R.C., Bellon, H., Drummond, M.S., Feigenson, M.D., and Jackson, T.E., 1991b, Dacite genesis via both slab melting and differentiation: Petrogenesis of La Yeguada volcanic complex, Panama: *Journal of Petrology*, v. 32, no. 6, p. 1101–1142.
- Dickinson, W.R., 1985, Interpreting provenance relations from detrital modes of sandstones, in Zuffa, G.G., ed., *Provenance of Arenites*: NATO ASI Series, C 148: Dordrecht, D. Reidel Publishing Company, p. 333–361.
- Donelick, R.A., and Miller, D.S., 1991, Enhanced TINT fission track densities in low spontaneous track density apatites using ^{252}Cf -derived fission track fragment tracks: A model and experimental observations: *International Journal of Radiation Applications and Instrumentation*, v. 18, Part D: Nuclear Tracks and Radiation Measurements, p. 301–307.
- Donelick, R.A., Ketcham, R.A., and Carlson, W.D., 1999, Variability of apatite fission-track annealing kinetics: II. Crystallographic orientation effects: *The American Mineralogist*, v. 84, p. 1224–1234.
- Donelick, R.A., O'Sullivan, P.B., and Ketcham, R.A., 2005, Apatite fission track analysis: Reviews in Mineralogy and Geochemistry, v. 58, no. 1, p. 49–94, doi:10.2138/rmg.2005.58.3.
- Duque-Caro, H., 1990, Neogene stratigraphy, paleoceanography and paleobiogeography in northwest South America and the evolution of the Panama Seaway: *Palaeogeography, Palaeoclimatology, Palaeoecology*, v. 77, p. 203–234.
- Farley, K.A., 2000, Mantle noble gas geochemistry: progress and problems: *Journal of Geophysical Research*, v. 105, no. B2, p. 2903–2914, doi:10.1029/1999JB900348.
- Farley, K.A., 2002, (U–Th)/He dating: Techniques, calibrations, and applications: Reviews in Mineralogy and Geochemistry, v. 47, p. 819–844, doi:10.2138/rmg.2002.47.18.
- Farris, D.W., Jaramillo, C.A., Bayona, G.A., Restrepo-Moreno, S.A., Montes, C., Cardona, A., Mora, A., Speakman, R.J., Glasscock, M.D., Reiners, P., and Valencia, V., 2011, Fracturing of the Panamanian

Middle Eocene and younger emergence of Panama

- isthmus during initial collision with South America: *Geology*, v. 39, p. 1007–1010, doi:10.1130/G32237.1.
- Fitzgerald, P.G., Baldwin, S.L., Webb, L.E., and O'Sullivan, P.B., 2006, Interpretation of (U-Th)/He single grain ages from slowly cooled crustal terranes: A case study from the Transantarctic Mountains of southern Victoria Land: *Chemical Geology*, v. 225, p. 91–120, doi:10.1016/j.chemgeo.2005.09.001.
- Galbraith, R., 1981, On statistical models for fission track counts: *Journal of the International Association for Mathematical Geology*, v. 13, p. 471–478, doi:10.1007/BF01034498.
- Galbraith, R., 2005, *The Statistics for Fission Track Analysis*: Boca Raton, Florida, Chapman & Hall/CRC, 240 p.
- Galbraith, R., and Laslett, G.M., 1993, Statistical models for mixed fission track ages: *Nuclear Tracks*, v. 21, p. 459–470.
- Gehrels, G., Valencia, V., and Pullen, A., 2006, Detrital zircon geochronology by laser-ablation multicollector ICPMS at the Arizona LaserChron Center: *The Paleontological Society Papers*, v. 12, p. 67–76.
- Gehrels, G., Valencia, V., and Ruiz, J., 2008, Enhanced precision, accuracy, efficiency, and spatial resolution of U-Pb ages by laser ablation-multicollector-inductively coupled plasma-mass spectrometry: *Geochemistry, Geophysics, Geosystems*, v. 9, no. 3, Q03017, doi:10.1029/2007GC001805.
- Gleadow, A.J.W., Duddy, I.R., Green, A.R., and Lovering, J.F., 1986, Confined fission track lengths in apatite: A diagnostic tool for thermal history analysis: *Contributions to Mineralogy and Petrology*, v. 94, p. 405–415, doi:10.1007/BF00376334.
- Graham, A., Stewart, R.H., and Stewart, J.L., 1985, Studies in Neotropical Paleobotany: III. The Tertiary communities of Panama—Geology of the pollen-bearing deposits: *Annals of the Missouri Botanical Garden*, v. 72, no. 3, p. 485–503, doi:10.2307/2399100.
- Green, P.F., Duddy, I.R., Gleadow, A.J.W., Tingate, P.R., and Laslett, G.M., 1985, Fission track annealing in apatite: Track length measurements and the form of the Arrhenius plot: *Nuclear Tracks*, v. 10, p. 323–328.
- Guidice, D., and Recchi, G., 1969, *Geología del Área del Proyecto Minero de Azuero: Programa para el Desarrollo de las Naciones Unidas, Informe Técnico preparado para el gobierno de la República de Panamá*, 53 p.
- Haug, G.H., Tiedemann, R., Zahn, R., and Ravelo, A.C., 2001, Role of Panama uplift on oceanic freshwater balance: *Geology*, v. 29, p. 207–210, doi:10.1130/0091-7613(2001)029<0207:ROPULO>2.0.CO;2.
- Hourigan, J.K., Reiners, P.W., and Brandon, M.T., 2005, U-Th zonation-dependent alpha-ejection in (U-Th)/He chronometry: *Geochimica et Cosmochimica Acta*, v. 69, p. 3349–3365, doi:10.1016/j.gca.2005.01.024.
- House, M.A., Farley, K.A., and Kohn, B.P., 1999, An empirical test of helium diffusion in apatite: Borehole data from the Otway Basin, Australia: *Earth and Planetary Science Letters*, v. 170, p. 463–474, doi:10.1016/S0012-821X(99)00120-X.
- House, M.A., Farley, K.A., and Stockli, D.F., 2000, Helium chronometry of apatite and titanite using Nd-YAG laser heating: *Earth and Planetary Science Letters*, v. 183, p. 365–368, doi:10.1016/S0012-821X(00)00286-7.
- Ingersoll, R.V., Bullard, T.F., Ford, R.L., Grimm, J.P., Pickle, J.D., and Sares, S.W., 1984, The effect of grain size on detrital modes: A test of the Gazzi-Dickinson point counting method: *Journal of Sedimentary Petrology*, v. 54, no. 1, p. 103–116.
- Jackson, J.B.C., Jung, P., Coates, A.G., and Collins, L.S., 1993, Diversity and extinction of tropical American mollusks and emergence of the Isthmus of Panama: *Science*, v. 260, no. 5114, p. 1624–1626, doi:10.1126/science.260.5114.1624.
- Jenkins, D.G., 1964, Panama and Trinidad Oligocene rocks: *Journal of Paleontology*, v. 38, no. 3, p. 606.
- Johnson, K.G., and Kirby, M.X., 2006, The Emperor limestone rediscovered: Early Miocene corals from the Culebra Formation, Panama: *Journal of Paleontology*, v. 80, no. 2, p. 283–293, doi:10.1666/0022-3360(2006)080[0283:TELREM]2.0.CO;2.
- Kameo, K., and Sato, T., 2000, Biogeography of Neogene calcareous nannofossils in the Caribbean and the eastern equatorial Pacific—Floral response to the emergence of the Isthmus of Panama: *Marine Micropaleontology*, v. 39, no. 1–4, p. 201–218, doi:10.1016/S0377-8398(00)00021-9.
- Keigwin, L.D., 1978, Pliocene closing of the Isthmus of Panama, based on biostratigraphic evidence from nearby Pacific Ocean and Caribbean Sea cores: *Geology*, v. 6, no. 10, p. 630–634, doi:10.1130/0091-7613(1978)6<630:PCOTIO>2.0.CO;2.
- Keigwin, L.D., 1982, Isotopic paleoceanography of the Caribbean and East Pacific: role of Panama uplift in late Neogene time: *Science*, v. 217, no. 4557, p. 350–353, doi:10.1126/science.217.4557.350.
- Kerr, A.C., Marriner, G.F., Tarney, J., Nivia, A., Saunders, A.D., Thirlwall, M.F., and Sinton, C.W., 1997, Cretaceous basaltic terranes in western Colombia: Elemental, chronological and Sr-Nd isotopic constraints on petrogenesis: *Journal of Petrology*, v. 38, no. 6, p. 677–702, doi:10.1093/petrology/38.6.677.
- Kesler, S.E., Sutter, J.F., Issigonis, M.J., Jones, L.M., and Walker, R.L., 1977, Evolution of porphyry copper mineralization in an oceanic island arc: Panama: *Economic Geology and the Bulletin of the Society of Economic Geologists*, v. 72, p. 1142–1153, doi:10.2113/gsecongeo.72.6.1142.
- Ketcham, R.A., 2005, Forward and inverse modeling of low-temperature thermochronometry data: Reviews in Mineralogy and Geochemistry, v. 58, p. 275–314, doi:10.2138/rmg.2005.58.11.
- Ketcham, R.A., 2008, *HeFTy: Viola, Idaho, Apatite to Zircon Inc.*, <http://ctlab.geo.utexas.edu/Ketcham/ft/>.
- Ketcham, R.A., Donelick, R.A., and Carlson, W.D., 1999, Variability of apatite fission-track annealing kinetics: III. Extrapolation to geological time scales: *The American Mineralogist*, v. 84, p. 1235–1255.
- Ketcham, R.A., Carter, A., Donelick, R.A., Barbarand, J., and Hurford, A.J., 2007, Improved measurement of fission-track annealing in apatite using *c*-axis projection: *The American Mineralogist*, v. 92, p. 789–798, doi:10.2138/am.2007.2280.
- Kirby, M.X., and MacFadden, B., 2005, Was southern Central America an archipelago or a peninsula in the middle Miocene? A test using land-mammal body size: *Palaeogeography, Palaeoclimatology, Palaeoecology*, v. 228, no. 3–4, p. 193–202, doi:10.1016/j.palaeo.2005.06.002.
- Kirby, M.X., Jones, D.S., and MacFadden, B.J., 2008, Lower Miocene stratigraphy along the Panama Canal and its bearing on the Central American Peninsula: *PLoS ONE*, v. 3, no. 7, e2791, doi:10.1371/journal.pone.0002791.
- Kolarsky, R.A., and Mann, P., 1995, Structure and neotectonics of an oblique-subduction margin, southwestern Panama, *in* Mann, P., ed., *Geologic and Tectonic Development of the Caribbean Plate Boundary in Southern Central America*: Geological Society of America Special Paper 295, p. 131–157.
- Kolarsky, R.A., Mann, P., and Monechi, S., 1995, Stratigraphic development of southwestern Panama as determined from integration of marine seismic data and onshore geology, *in* Mann, P., ed., *Geologic and Tectonic Development of the Caribbean Plate Boundary in Southern Central America*: Geological Society of America Special Paper 295, p. 159–200.
- Lear, C.H., Rosenthal, Y., and Wright, J.D., 2003, The closing of a seaway: Ocean water masses and global climate change: *Earth and Planetary Science Letters*, v. 210, p. 425–436, doi:10.1016/S0012-821X(03)00164-X.
- Lissina, B., 2005, A Profile through the Central American Landbridge in Western Panama: 115 Ma Interplay between the Galápagos Hotspot and the Central American Subduction Zone [Ph.D. dissertation]: Kiel, Germany, Christian-Albrechts Universität, 102 p.
- Lonsdale, P., 2005, Creation of the Cocos and Nazca plates by fission of the Farallon plate: *Tectonophysics*, v. 404, no. 3–4, p. 237–264, doi:10.1016/j.tecto.2005.05.011.
- Ludwig, K.J., 2007, *Isoplot 3.62*: Berkeley Geochronology Center Special Publication, 70 p.
- MacFadden, B.J., 2006, North American Miocene land mammals from Panama: *Journal of Vertebrate Paleontology*, v. 26, no. 3, p. 720–734, doi:10.1671/0272-4634(2006)26[720:NAMLMF]2.0.CO;2.
- MacFadden, B.J., Kirby, M.X., Rincon, A., Montes, C., Morón, S., Strong, N., and Jaramillo, C., 2010, Extinct Peccary “Cynorca” Occidentale (Tayassuidae, Tayassuinae) from the Miocene of Panama and correlations to North America: *Journal of Paleontology*, v. 84, no. 2, p. 288–298, doi:10.1666/09-064R.1.
- Mann, P., and Corrigan, J., 1990, Model for late Neogene deformation in Panama: *Geology*, v. 18, no. 6, p. 558–562, doi:10.1130/0091-7613(1990)018<0558:MFLNDI>2.3.CO;2.
- Mann, P., and Kolarsky, R.A., 1995, East Panama deformed belt: Structure, age, and neotectonic significance, *in* Mann, P., ed., *Geologic and Tectonic Development of the Caribbean Plate Boundary in Southern Central America*: Geological Society of America Special Paper 295, p. 111–130.
- Marshall, L.G., Webb, S.D., Sepkoski, J.J., and Raup, D.M., 1982, Mammalian evolution and the Great American Interchange: *Science*, v. 215, no. 4538, p. 1351–1357, doi:10.1126/science.215.4538.1351.
- Maury, R.C., Defant, M.J., Bellon, H., De Boer, J.Z., Stewart, R.H., and Cotten, J., 1995, Early Tertiary arc volcanics from eastern Panama, *in* Mann, P., ed., *Geologic and Tectonic Development of the Caribbean Plate Boundary in Southern Central America*: Geological Society of America Special Paper 295, p. 29–34.
- Molnar, P., 2008, Closing of the Central American Seaway and the ice age: A critical review: *Paleoceanography*, v. 23, PA2201, doi:10.1029/2007PA001574.
- Montes, C., Guzman, G., Bayona German, A., Cardona, A., Valencia, V., and Jaramillo Carlos, A., 2010, Clockwise rotation of the Santa Marta massif and simultaneous Paleogene to Neogene deformation of the Plato San Jorge and Cesar Rancheria basins: *Journal of South American Earth Sciences*, v. 29, p. 832–848, doi:10.1016/j.jsames.2009.07.010.
- Newkirk, D.R., and Martin, E., 2009, Circulation through the Central American Seaway during the Miocene carbonate crash: *Geology*, v. 37, no. 1, p. 87–90, doi:10.1130/G25193A.1.
- O'Sullivan, P.B., and Parrish, R.R., 1995, The importance of apatite composition and single-grain ages when interpreting fission track data from plutonic rocks: A case study from the Coast Ranges, British Columbia: *Earth and Planetary Science Letters*, v. 132, p. 213–224, doi:10.1016/0012-821X(95)00058-K.
- Pindell, J.L., and Kennan, L., 2009, Tectonic evolution of the Gulf of Mexico, Caribbean and northern South America in the mantle reference frame: An update, *in* James, K.H., Lorente, M.A., and Pindell, J.L., eds., *The Origin and Evolution of the Caribbean Plate*: Geological Society of London Special Publication 328, p. 1–55.
- Reiners, P., 2005, Zircon (U-Th)/He thermochronometry: Reviews in Mineralogy and Geochemistry, v. 58, no. 1, p. 151–179, doi:10.2138/rmg.2005.58.6.
- Restrepo-Moreno, S.A., Foster David, A., Stockli Daniel, F., and Parra-Sanchez Luis, N., 2009, Long-term erosion and exhumation of the “Altiplano Antioqueño,” Northern Andes (Colombia) from apatite (U-Th)/He thermochronology: *Earth and Planetary Science Letters*, v. 278, p. 1–12, doi:10.1016/j.epsl.2008.09.037.
- Retallack, G.J., and Kirby, M.X., 2007, Middle Miocene global change and paleogeography of Panama: *Palaios*, v. 22, no. 6, p. 667–679.
- Rooney, T., Franceschi, P., and Hall, C., 2010, Water saturated magmas in the Panama Canal region—A precursor to adakite-like magma generation?: Contributions to Mineralogy and Petrology, v. 161, p. 373–388, doi:10.1007/s00410-010-0537-8.
- Rubatto, D., 2002, Zircon trace element geochemistry: Distribution coefficients and the link between U-Pb ages and metamorphism: *Chemical Geology*, v. 184, p. 123–138, doi:10.1016/S0009-2541(01)00355-2.
- Shelton, B.J., 1952, *Geology and Petroleum Prospects of Darien, Southeastern Panama* [M.Sc. thesis]: Corvallis, Oregon, Oregon State College, 67 p.
- Silver, E.A., Reed, D.L., Tagudin, J.E., and Heil, D.J., 1990, Implications of the north and south Panama thrust belts for the origin of the Panama orocline: *Tectonics*, v. 9, no. 2, p. 261–281, doi:10.1029/TC009i002p00261.
- Speidel, F., Faure, S., Smith, M.T., and McArthur, G., 2001, *Exploration and Discovery at the Petaquilla Copper*

- Gold Concession, Panama, in Albison, T., and Nelson, C.E., eds., *New Mines and Discoveries in Mexico and Central America*: Society of Economic Geologists Special Publication, no. 8, p. 349–362.
- Stacey, J.S., and Kramers, J.D., 1975, Approximation of terrestrial lead isotope evolution by a two-stage model: *Earth and Planetary Science Letters*, v. 26, no. 2, p. 207–221, doi:10.1016/0012-821X(75)90088-6.
- Stewart, R.H., Stewart, J.L., and Woodring, W.P., 1980, *Geologic Map of the Panama Canal and Vicinity*, Republic of Panama: U.S. Geological Survey Miscellaneous Investigations Series Map I-1232, scale 1:100,000, 1 sheet.
- Terry, R.A., 1956, *A Geological Reconnaissance of Panama*: California Academy of Sciences Occasional Paper 23, 91 p.
- Tripathi, A., and Zachos, J., 2002, Late Eocene tropical sea surface temperatures: A perspective from Panama: *Paleoceanography*, v. 17, no. 3, p. 1–14, doi:10.1029/2000PA000605.
- Valencia, V.A., Ruiz, J., Barra, F., Gehrels, G., Ducea, M., Titley, S.M., and Ochoa-Landin, L., 2005, U-Pb single zircon and Re-Os geochronology from La Caridad porphyry copper deposit: Insights for the duration of magmatism and mineralization in the Nacozari District, Sonora, Mexico: *Mineralium Deposita*, v. 40, p. 175–191, doi:10.1007/s00126-005-0480-1.
- van der Plas, L., and Tobi, A.C., 1965, A chart for judging the reliability of point counting results: *American Journal of Science*, v. 263, p. 87–90, doi:10.2475/ajs.263.1.87.
- Wadge, G., and Burke, K., 1983, Neogene Caribbean plate rotation and associated Central American tectonic evolution: *Tectonics*, v. 2, no. 6, p. 633–643, doi:10.1029/TC002i006p00633.
- Wegner, W., Wörner, G., Harmon, M.E., and Jicha, B.R., 2011, Magmatic history and evolution of the Central American land bridge in Panama since the Cretaceous times: *Geological Society of America Bulletin*, v. 123, no. 3/4, p. 703–724, doi:10.1130/B30109.1.
- Weigt, L.A., Crawford, A.J., Rand, S., and Ryan, M., 2005, Biogeography of the Túngara frog, *Physalaemus pustulosus*: A molecular perspective: *Molecular Ecology*, v. 14, p. 3857–3876, doi:10.1111/j.1365-294X.2005.02707.x.
- Westbrook, G.K., 1990, Gravity anomaly map of the Caribbean region, in Dengo, G., and Case, J.E., eds., *The Caribbean Region*: Boulder, Colorado, Geological Society of America, *The Geology of North America*, v. H, plate 7.
- Whitmore, F.C., Jr., and Stewart, R.H., 1965, Miocene mammals and Central American seaways: Fauna of the Canal Zone indicates separation of Central and South America during most of the Tertiary: *Science*, v. 148, no. 3667, p. 180–185, doi:10.1126/science.148.3667.180.
- Woodring, W.P., 1957, *Geology and Description of Tertiary Mollusks (Gastropods; Trochidae to Turritellidae): Geology and Paleontology of Canal Zone and Adjoining Parts of Panama*: U.S. Geological Survey Professional Paper 306-A, 145 p.
- Woodring, W.P., 1982, *Geology and Paleontology of Canal Zone and Adjoining Parts of Panama*: Description of Tertiary Mollusks; Pelecypods, Propeamussiidae to Cuspidariidae; Additions to Families Covered in P 306-E; Additions to Gastropods; Cephalopods: U.S. Geological Survey Professional Paper 306–7, p. 541–759.
- Wörner, G., Harmon, R., and Wegner, W., 2009, Geochemical evolution of igneous rock and changing magma sources during the formation and closure of the Central American land bridge of Panama, in Kay, S.M., Ramos Victor, A., and Dickinson, W.R., eds., *Backbone of the Americas: Shallow Subduction, Plateau Uplift, and Ridge and Terrane Collision*: Geological Society of America Memoir 204, p. 183–196.

SCIENCE EDITOR: A. HOPE JAHREN
ASSOCIATE EDITOR: STEPHEN T. JOHNSTON

MANUSCRIPT RECEIVED 7 APRIL 2011
REVISED MANUSCRIPT RECEIVED 1 OCTOBER 2011
MANUSCRIPT ACCEPTED 19 OCTOBER 2011

Printed in the USA